Corrugated Wall Effects in Vertical Concentric Ground-Source Heat Pumps

---

2011-2012 WPI MQP Project Report

Brendan M. Hamm, Worcester Polytechnc Institute
Kaj R. Peterson, Worcester Polytechnic Institute

Date: April 25, 2012

Approved:

Professor B.S. Tilley, Advisor

Abstract

For the past thirty years ground source heat pumps (GSHPs) utilized the near constant subsurface temperature to control the climate of residences. The high cost of installation compared to traditional systems has prevented their widespread adoption as a climate control system. However, the operational costs of such systems are less than traditional systems. We consider vertical concentric GSHPs. These systems consist of an inner pipe which transports fluid from the residence to the bottom of the well. The fluid then returns to the residence through the annular gap between this inner pipe and the borehole casing. Current systems utilize a corrugation at the outer most section of the inner pipe in an attempt to improve heat transfer within the system. We consider the case with the corrugated boundary in Cartesian coordinates. We utilize the Navier-Stokes equation for incompressible Newtonian fluid flow and the conservation of energy equation within the annular gap under the assumptions of no heat flux between the inner and annular pipe, and no-slip and periodicity conditions on the boundary to develop our model. We non-dimensionalize the equations and apply perturbation theory to find leading order differential equations for fluid flow and heat transfer within a singular period of corrugation. Over this single period we find the amplitude of corrugation to have an effect on the heat transfer, however with an increasing number of periods the effect diminishes. These same methods are then applied to the system utilizing homogenization techniques over the full length of the pipe. We find that over several periods of corrugation the steady state temperature solution is independent of the amplitude of this corrugation for laminar flow profiles. A comparison of these asymptotic results to COMSOL simulations are considered.

Acknowledgements

Contents

Chapter 1

Introduction

One of the largest concerns of our world today is energy, as the reserves of oil and gas are depleted and demand for affordable energy increases. Fossil fuels account for over 80% of the energy supply in the U.S., however there exists only a finite supply of such fuels. In the 1950's a geophysicist M. King Hubbert developed a model to describe the interrelation between oil production and supply. Hubbert concluded that an oil crisis occurs when production out-paces demand, not when supplies are exhausted. When Hubbert formulated his theory he applied it to U.S. supplies and predicted 1970 would be the year at which U.S. production reached its peak [25]. Hubbert's prediction has been realized as oil production in the U.S. has been decreasing since its peak in 1970, despite discovery of many more oil fields [57]. Due to this decline in fossil fuel production it is imperative that alternatives be found and researched.

The U.S. Department of Energy Quadrennial review states 6 goals for the energy sector including reducing oil use by 33% and increasing usage of renewable resources [56]. The current breakdown of energy usage is: Petroleum 37%, Natural Gas 25%, Coal 21%, Nuclear 9%, Renewable Energy 8%. The breakdown of Renewable Energy is: Hydro-power 31%, Wood Burning 25%, Biofuels 23%, Wind 11%, Biomass Waste 6%, Geothermal 3%, and Solar 1%. As of 2010 the annual energy demand in the U.S. totaled 98 quadrillion Btu, of which only 75% is derived from domestic production [43, 57].

One of the major drawbacks of using fossil fuels for our energy needs stems from the damage caused by introducing large levels of chemicals into our environment. Combustion of fossil fuels creates several greenhouse gases such as CO_2, CH_4, N_2O, $HFCs$, $PFCs$, and SF_6 [43]. These gases act to trap solar radiation within our atmosphere, and this trapped radiation may cause climate change. In addition to the detrimental effects of burning fossil fuels there is also the problem of production/transportation associated environmental impacts such as the Gulf Oil Spill, Exxon-Valdez, and hydrofracking contamination. Of all current energy sources, geothermal systems have the least negative environmental impact and with more widespread use could become an integral part in lowering CO_2 emissions [43, 44, 29].

In addition to having negative environmental impacts, the cost of petroleum products has been steadily rising over the past several decades. In 2010 the price of crude oil passed the important psychological price of $100/barrel and remained above this marker for all but brief periods of time throughout 2011. In the past the United States' reliance on foreign oil, coupled with decisions by

OPEC has resulted in gas rationing which occurred in the oil shortage of 1973 [25]. The production and use of renewable fuels has grown more quickly in recent years as a result of higher prices for oil and natural gas, and a number of State and Federal Government incentives, including the Energy Policy Acts of 2002 and 2005. The use of renewable fuels is expected to continue to grow over the next 30 years, as research continues to make these technologies more efficient and cost effective [37, 57].

While currently the costs associated with producing energy from renewable resources are greater than those for fossil fuels, they aid in reducing costs of fossil fuels, a basic functionality of supply and demand. However, as reusable energy sources become more prevalent the associated costs should be reduced. In addition, many of these renewable technologies are still relatively new and continued research will work to increase their efficacy while also reducing costs [37, 18].

In the U.S. heating requirements account for 41% of total energy usage, rendering it one of the largest sectors of energy consumption. "Due to the longer heating seasons, the Northeast and Midwest regions consume the most energy per household, at 123 and 110 Million Btu per household in 2005, respectively." [57] Due to this large consumption of energy specifically for heating purposes alternative technologies and improvements in this area have great potential for reducing dependence on fossil fuels.

One such technology with limited prior interest is geothermal energy. Geothermal energy can be used for several purposes, including electrical energy production and direct heating of buildings, however current research focuses primarily on the latter. It makes up only a small percentage of total energy production and utilization, however due to rising prices of fossil fuels interest has increased over the past decade. "World geothermal energy installed capacity at the end of 2009 was 10.7 gigawatts (GW_e) for electricity generation and 50.6 GW_{th} for direct use. Approximately 67 terawatt hours (TWh) of base-load electricity were generated with typical capacity factors of 75%. Almost 440 petajoules (PJ) of direct heat were used, with Ground Source Heat Pumps (GSHPs) the largest contributor at about 50% [29]." In Figure 1.1 we see the annual cost comparison of operating a geothermal system compared to traditional fossil fuel based systems. As can be readily seen the costs associated with operating a geothermal system are between 25% - 30% that of highly efficient natural gas and propane systems, with oil heating being even more costly. Additionally, while fossil fuel based furnaces require regular maintenance and cleaning, GSHPs typically only require filter changes and pressure tests on an annual basis [47]. Maintenance costs (combined log mean annual service/maintenance cost) range from 6.73-9.21 cents/ft^2 which is approximately \$200-\$300 for 3000 ft^2 home annually [37].
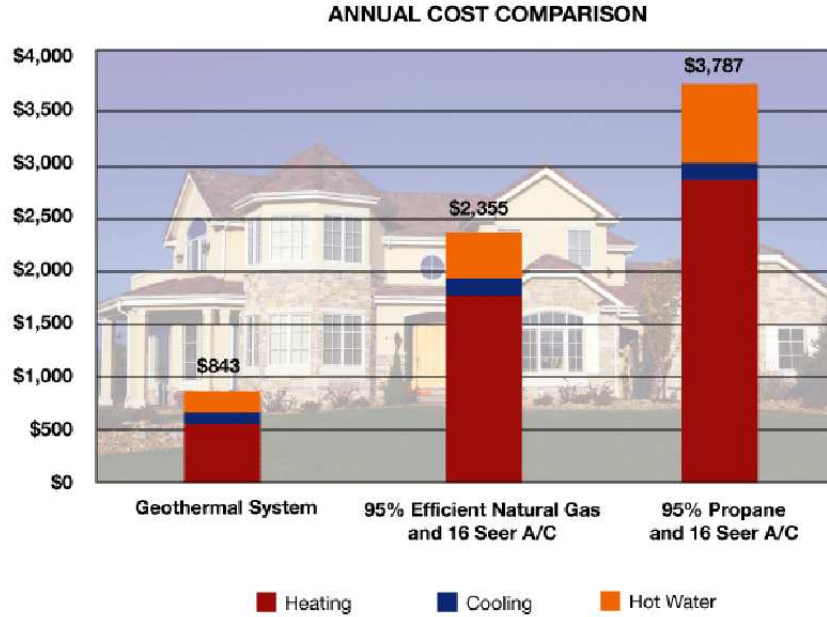
Figure 1.1: Annual Cost Comparison [41]

The reason for this large difference in cost is largely due to the difference in efficiency between the systems. All GSHPs are based upon the laws of thermodynamics, and function by way of a Carnot Cycle. The efficiency of these systems is measured by the Carnot Coefficient of Performance (COP_{Carnot}) and the Energy Efficiency Ratio (EER), given below [42].

$$COP_{Carnot} = \frac{T_H}{T_H - T_L}$$

$$EER = \frac{\text{Cooling Output}(Btu)}{\text{Electrical Input}(Wh)}$$

In order to show why geothermal systems are more efficient mathematically we must first understand how they function. In Figure 1.2 we see the subsurface temperatures plotted vs. depth in the ground over various seasons. As can be seen, the ground temperature 5 meters below the surface is generally constant, varying by only a few degrees Celsius, depending on geographical location [43, 40].

The reason for this semi-constant ground temperature is due to the fact that heat is transferred very slowly through soil; that is not to say there is only a small quantity of energy within the soil. "An estimated 1% of heat from upper 8 km of earth's crust is more than 250 times the energy of all crude and nat. gas reserves [55]." Due to this small annual temperature difference in the soil and by looking at the calculation of the COP_{Carnot} it is easy to see that we can achieve higher efficiencies with geothermal systems than is possible for traditional fossil fuel systems [43, 24]. Currently geothermal systems have the highest efficiency of any current system with a $COP \approx 4$; in contrast even the best fossil fuel systems have a $COP \approx 0.9$. The EER of boilers and furnaces

3

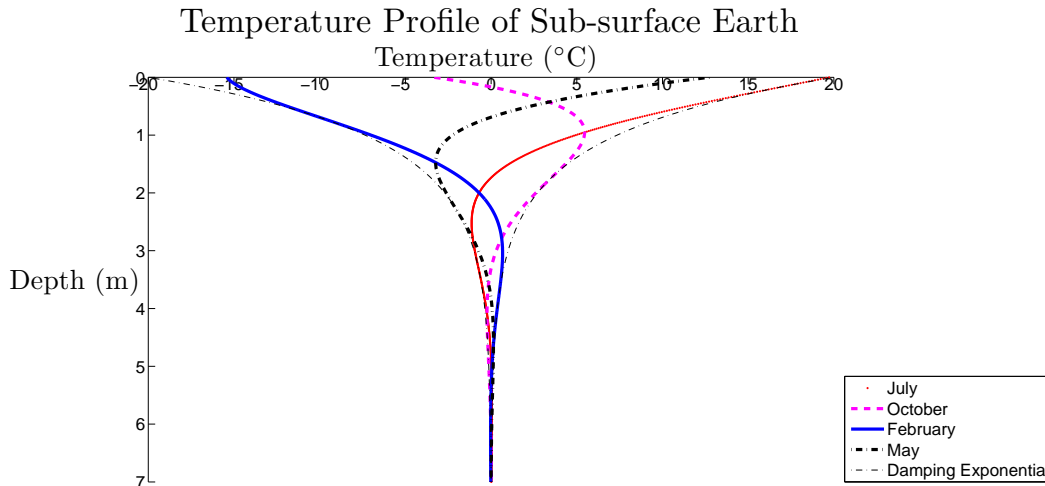## Temperature Profile of Sub-surface Earth

Temperature (°C)

Figure 1.2: Subsurface Temperature Profile [17]

range between 11-15 whereas geothermal systems are rated between 20-30. This translates to a 45%-50% reduction in power consumption. Assuming a system has a $COP \approx 4$ and with a cost of electricity of $0.13/kWh, the cost to run such a system is about $953 per year [40]. GSHP systems are at their maximum potential in areas with large climatic differences throughout the year as they are able to take full advantage of the semi-constant ground temperature. Unsurprisingly, the majority of GSHPs in use may be found in such areas; a report by Lienau [39] states that geothermal systems are primarily used for residential purposes in areas with moderate to severe winters.

There are several different types of GSHPs,separated in two major categories: open-loop and closed-loop systems. Within closed-loop there are two orientations: vertical and horizontal. Different in-situ requirements determine which type is most advantageous in each specific case. We give the reader a brief overview of each type of GSHP, how they function, and their individual characteristics.

Open loop systems function by piping water from an underground aquifer or stream into a heat exchanger by means of a pump. The heat exchanger then transfers heat to or from the water into the space, depending on the season, and the water is returned to the aquifer via a separate pipe. Open loop systems are slightly more efficient than closed loop systems because there are fewer heat transfer steps, however there is an additional environmental concern in utilizing a subterranean aquifer directly [1]. The environmental concerns are primarily introduction of alien chemicals or other substances into the aquifer and the effect of the changing temperature of the surrounding environment over longer periods of time. The most obvious limiting factor of open loop systems is the requirement of a subterranean aquifer. Artificial aquifers have been constructed but their cost is high and there have been problems with excessive water pressures damaging the systems [47, 5].

Closed loop GSHPs function similarly to open loop systems with one key difference; rather

than the fluid being taken from an aquifer, a fluid is circulated through a closed network of pipes oriented either horizontally or vertically beneath the ground. Throughout this circulation process heat transfer takes place between the fluid, the grout filler, and soil surrounding the piping. The pipes must be of sufficient length and/or depth that the desired amount of heat transfer occurs. The typical lengths are comparatively long due to the inherently low thermal transfer efficiency between a fluid in a pipe and the surrounding soil via a conducting grout, the transfer efficiency being dominated the the properties of the soil [49, 44]. We provide simple diagrams outlining how each system is placed in relation to the building in Figure 1.3.
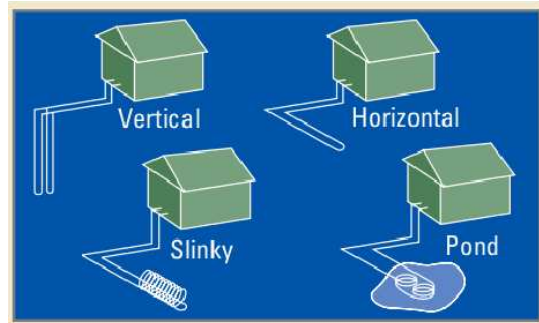

Figure 1.3: Closed Loop GSHP Configurations [43]

Cycling from top left in a clockwise manner we have a vertical U-tube system, a simple horizontal system, a pond system, and a horizontal slinky system. We will discuss the two major orientations as the pond and slinky system utilize the same general principles as the simple horizontal system. Of the two orientations, horizontal systems are typically more cost effective than their vertical counterparts. Depths at which horizontal systems are installed allow for excavation rather than drilling, reducing their installation cost, but leaving them more vulnerable to damage. They require about $9000\,\mathrm{ft}^2$ of land for the piping, which is placed between 6-10 ft below the surface. One advantage is that the excavation requirements of building construction (water, electricity, etc.) can be dually utilized for installation of the geothermal system, further reducing the costs associated for new construction projects [40]. The close proximity to the surface slightly reduces the functional efficiency due to the greater variation in ground temperature closer to the surface [16]. In addition, to achieve maximum efficiency nothing may be placed over the ground in which the piping lies, making the land above of limited use [21].

Vertical loop systems are used when horizontal systems are unsuitable and are essentially identical to horizontal systems, with only vertical bore-holes used instead of a horizontally oriented piping field. The depth of these bore-holes ranges from 100-300 ft and each system requires between 1-10 bore-holes depending on the size of the building and the intended purpose of the system. Each bore-hole is spaced approximately 10-20 ft apart, requiring far less space than horizontal systems, making them ideal for urban areas. Another advantage of the vertical systems is the more constant ground temperature due to depth, improving the overall efficiency of the system. However a seasonal load imbalance can alter the local ground temperature after several years by up to 5 °C, drastically reducing efficiency of geothermal systems [38]. U-tube systems are a specific type of

vertical GSHP that is simply a pipe running through the bore-hole with a U-bend at the bottom of the bore-hole, with a bore-hole diameter 3-5 inches [3]. However, U-tube systems require sufficient space between the pipes, increasing the required area for the systems efficient operation [10, 4]. Vertical concentric systems are suited for areas with high population density, thus the large advantage of the concentric design is its minimal space requirement. Unlike the U-tube design the entire exchange is contained within 1 pipe; the fluid flows from the building into the ground through a center pipe called the core, and the fluid returns around an outer annular pipe called the return [15]. The systems are slightly more expensive than U-tube systems due to their specialization however they require even less space and are prone to less problems. A typical U-tube vertical system requires 200-400 ft^2 per ton whereas horizontal system requires 2000-3500 ft^2 per ton [9]. Concentric vertical pipes further reduce the amount of surface area required for drilling to 120-240 ft^2 per ton [9]. In Figure 1.4 we provide a diagram of a concentric GSHP system.
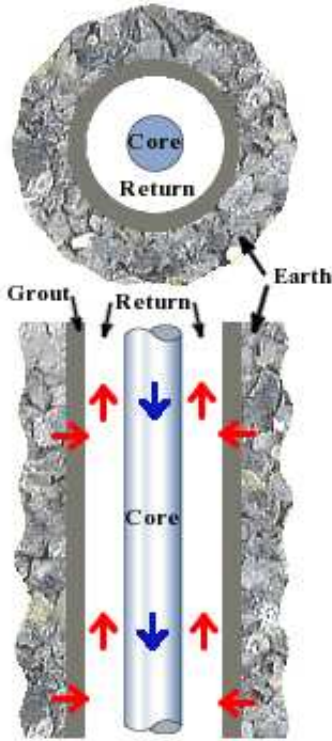

Figure 1.4: Vertical Concentric GSHP

There are several factors which hamper the ability of geothermal systems from becoming a widespread source of alternative heating. Among them the length of time to achieve payback is certainly the biggest detractor to potential end users and contractors. The federal government and several states currently offer several incentive plans to increase the rate of geothermal installations as well as other alternative fuel and heat sources [29]. However, due to current installation costs, such incentive plans have little effect on changing heating/cooling systems in existing homes but rather influence system choice in new constructions [47]. The most important issue preventing widespread use of geothermal systems is the high installation cost, particularly due to drilling for the vertical systems. Depending on local geological conditions the cost of drilling is $100/ft linearly, with costs rising for bedrock or unfavorable drilling conditions. As mentioned before with bore-hole running anywhere from 100-300ft the costs for drilling alone are about $10,000 to $30,000 depending on the design capacity of the system, the type of system, and several other in-situ factors [40]. With current economic conditions taken into account for traditional heating systems and the cost of fossil fuels; the installation and minimal operation costs of geothermal systems require about 10 years to pay itself off, which is currently longer than the average home-owner expectancy per house. The typical cost of installation of a vertical system is currently $2,999-$4,400 per ton, while horizontal systems cost $2,712-$4,000 per ton [31, 46]. The size of the system required varies by heating/cooling requirements of the region, the size of the structure in question, and the insulation of the structure. However, in general a $3,000\,\text{ft}^2$ home would require a 3-5 ton system [31]. Thus, the total installation cost for a $3,000\,\text{ft}^2$ home is estimated to be in the range of $9,000-$22,000. In order for new and existing homes to begin to adopt geothermal systems, costs as well as payoff periods must be reduced. As the maintenance and operational costs are already very low, improvements in installation costs are imperative [9, 56]. The most efficient way to reduce installation costs is primarily in drilling depth. By increasing the heat transfer efficiency per foot of piping we can reduce the costs by a significant margin, allowing for more widespread adoption of the systems. Mathematical modeling of these systems allows us to explore different approaches to solve this problem in a variety of manners, a few described briefly below and the interested reader may find more information in the respective papers. According to a report by the US Department of Energy, the need to develop analytical and computational models to understand multiphysics and multi-scale phenomena, as well as mathematical techniques for decomposing complex systems, are among the top priorities for energy research for the future. These models are not only needed to improve upon energy technologies, but also to inform policy decisions [18]. In addition to reducing installation costs, numerical models to predict the performance of such systems have a greater error rate with increasing bore-hole depths [12].

Over the past several decades research has been done to improve the efficiencies and reduce the costs associated with GSHPs. Much work has been conducted in the areas of bore-hole depth, grouting materials, pipe orientation, soil temperature change, and thermal interaction between pipes. As drilling accounts for approximately half of the installation costs, reducing the depth of a bore-hole is an area for improvement. One study looked at independently optimizing a number of such parameters using an antifreeze solution and found slight differences in performance but concluded more study would be required to determine if such optimization can be achieved [33]. Another such study looked at the effects of using aluminum finned piping and concluded

use of aluminum finned piping was able to reduce required piping length for the same size system as traditional piping, allowing for lower excavation or drilling costs [34]. In order to reduce the total depth requirement of a system, the transfer rate of heat between the pipes and ground must be increased.

One area of research has been on increasing the heat transfer of the pipes through various geometrical changes. Early research focused on modeling the diffusion of a solute in a fluid flowing through a tube. Research by Sir Geoffrey Taylor [53, 54] sought to accurately model the dispersion of soluble matter injected into a slowly moving fluid within a pipe using non-dimensionalization techniques and comparing their predictions against experiments. A paper by Aris [8] removed the restrictions imposed by Taylor in his research concerning modeling of soluble matter dispersion by describing the distribution of solute in terms other than its moments in the direction of flow, allowing for much more general results. Research by Ahn examines the effects of corrugation and pipe diameter on the core tube and the effects on Nusselt and Reynolds numbers [2]. An analysis of the effect of thermal boundary conditions in rib-roughened passages was undertaken by Iaccarino et al. and determined that in a ribbed passage the heat transfer in strongly affected by convection upstream of the ribbing and by conduction downstream [27]. Another report by Iacovides et al. explored the effect of correction terms in two-dimensional rib-roughened passages with low Reynolds numbers. Two different models were tested with different correction terms and the authors found the correction terms overestimate the Nusselt number and do not fully reproduce corresponding measurements [28]. Bi et al. created a vertical, concentric model in which the return pipe coils helically around the core pipe. In this modeling increased heat transfer occurs in the bore-hole due to the increased surface area of the return. Utilizing their model they achieve errors averaging $0.62\,^{\circ}$C [15]. While many of these studies have found an increased heat transfer, work by Bohm suggests that the error bounds in modeling thermal flux underground increase for non-circular pipes [16].

Since the thermal conductivity of soil can vary greatly throughout a single bore-hole, it becomes necessary to attempt to homogenize the thermal conductivity. In an attempt to do this grouts with good thermal conductivity are used. Work done by Allan et al. has concluded that a cement silica sand grout can significantly reduce bore-hole depths. These cement silica sand grouts have thermal conductivities in the range 2.161-2.531 W/mK [6]. In addition research has shown that the thermal properties of the backfill material strongly affect the thermal resistance of a bore-hole [30].

In many systems, several bore-holes are required to achieve the levels of heating/cooling required for its intended building. When several different pipes are removing/replacing heat into the soil, they begin to interfere with the heat transfer of nearby pipes. If pipes are too close, this interaction can become significant and reduce the overall efficiency of the system and potentially render the system unable to meet peak demands needs of the building [11]. If the distance between pipes is made too great, the land requirement may again make the system unfeasible. Much work has been done over the past couple decades to model this interaction, and thus there is limited room for improvement utilizing this feature alone [3]. Most models in use today utilize a mid-point temperature average for the soil temperature [11]. Other work by Bandos et al. utilizes multiple time frames and the temperature is allowed to oscillate in a time-dependent fashion. While such a mod-

eling produces more accurate results, it also adds more complexity to the problem [10]. Works by Carli and Demir have led to the conclusion that the effects of surface temperature can be negated in bore-holes with depths exceeding 50 meters [21, 20]. Work by Esen et al. gives us data related to thermal conductivity and resistance within U-Tube vertical bore-holes over various depths, as well as conditions in which grout filler may be used to increase system efficiency [22]. Work by Lamarche et al. gives a new model for the short-term transient bore-hole problem which correlates with the numerical simulation as well as an addition to the finite line-source model dealing with average bore-hole temperature rather than the temperature at the bore-hole midpoint [35, 36].

Our work begins with a model used in a Summer 2011 REU project by Boyer et al. [17]. The objectives of this paper were to model a simple concentric GSHP system in radial coordinates and to determine which processes dominate the heat transfer within the system. Additionally the authors sought to describe the temperature change in terms of the pipe length. They found the heat transfer coefficient to dominate heat transfer and that reducing the return pipe radius significantly increases heat transfer.

We expand upon the REU research by assuming a sinusoidal corrugation along the inner return pipe wall in order to assess whether it has any effect on the heat transfer within the system. We will look at our chosen problem over two length scales; one period of corrugation (Chapters 2 and 3), and over the full length of the pipe (Chapter 4). In order to solve our problem over a single period of corrugation we apply the technique of non-dimensionalization in Chapter 2 with the aim of isolating the dominant processes effecting heat transfer within our system as well as to simplify calculation. We then apply Perturbation Theory and a Crank-Nicolson finite difference scheme in Chapter 3 to approximate solutions to our leading order fluid and heat transfer problems. The fluid flow problem will be solved under steady-state conditions whereas the heat problem will be time-dependent. In order to explore how our problem behaves over the entire length of the pipe we apply Homogenization in space to our problem and compare our results with those from our single corrugation period solutions in Chapter 4. In order to simplify our Homogenization problem we only treat the steady-state case in this paper. Finally we utilize the COMSOL multiphysics platform to model our system and compare its results to our homogenization solution in an attempt to validate the accuracy of our models. Our conclusions concerning our models and their respective results are outlined in Chapter 5.

Chapter 2

Model Formulation

We look at a 2-dimensional Cartesian analogue of the axially symmetric problem as a simplification of the full 3-dimensional problem. The problem was analyzed over two length scales; over a single period of corrugation λ, defined by a periodic function of z given as

$$h(z) = h_0 + a\sin(z), \tag{2.1}$$

and over the entire length of the pipe L as pictured on the left in Figure 2.1. It is important to note that h_0 represents the average annular gap while a denotes the amplitude of corrugation.
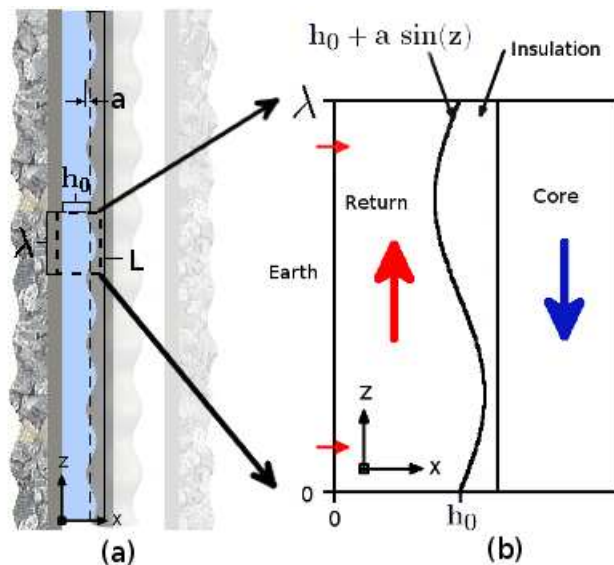

Figure 2.1: 2-d Corrugated Return Pipe Model

We assume homogeneous Neumann conditions between periods of corrugation and Newton's law of cooling to describe the diffusion of heat through the soil/grout surrounding the outer return wall defined at $x = 0$. Perfect thermal insulation is assumed along the corrugation at $x = h(z)$.

Additionally at a molecular level, fluid flow at the walls of the pipe ceases and thus we introduce a no-slip boundary condition [48]. In our model $z = 0$ corresponds to the base of the bore-hole. Below we outline our boundary conditions as stated respectively.

$$-k_0 T_x = \eta_0(T_{ext} - T) \quad \text{on} \quad x = 0. \tag{2.2}$$

$$\nabla T \cdot \hat{\mathbf{n}} = 0 \quad \text{on} \quad x = h(z). \tag{2.3}$$

$$\mathbf{u} = \mathbf{0} \quad \text{on} \quad x = 0. \tag{2.4}$$

$$\mathbf{u} = \mathbf{0} \quad \text{on} \quad x = h(z). \tag{2.5}$$

We use an incompressible fluid within our system thus we utilize the Navier-Stokes equations for incompressible Newtonian fluids. Below we outline our directionalized fluid flow where $\mathbf{u}$ represents the total fluid flux in our pipe, with u the radial flow as a function of x and z and w the vertical flow as a function of the same variables.

$$\mathbf{u} = u(x,z)\hat{\imath} + w(x,z)\hat{k}. \tag{2.6}$$

The following Navier-Stokes equations are the conservation of mass as well as the conservation of momentum equation for fluids [48].

$$\nabla \cdot \mathbf{u} = 0, \tag{2.7}$$

$$\rho\left[\mathbf{u}_t + \mathbf{u} \cdot \nabla \mathbf{u}\right] = -\nabla \tilde{p} + \mu \triangle \mathbf{u} + \rho \mathbf{g} \tag{2.8}$$

where ρ is the fluid density, $\tilde{p}$ is the pressure, μ is the dynamic viscosity, and $\mathbf{g}$ is gravity. Since $\rho \mathbf{g} = G$ for some scalar G we can simply define $p = \tilde{p} + G$ and retain equivalence. Equation (2.8) can now be written as in (2.9).

$$\rho\left[\mathbf{u}_t + \mathbf{u} \cdot \nabla \mathbf{u}\right] = -\nabla p + \mu \triangle \mathbf{u}. \tag{2.9}$$

The conservation of energy equation is given below, and is subsequently derived for heat transfer in a moving fluid.

$$\rho c_p T_t = -\nabla \cdot \mathbf{q}. \tag{2.10}$$

Here $\mathbf{q}$ is the heat flux. In a solid body the heat flux is proportional to $-k_0 \nabla T$ where k_0 is the thermal conductivity. However, in a moving fluid with velocity $\mathbf{u}$ the heat being transferred via advection is an additional flux term, such that

$$\mathbf{q} = \rho c_p T \mathbf{u} - \nabla T, \tag{2.11}$$

which gives us the conservation of energy equation for a moving fluid; ρ represents density, c_p is specific heat, and k_0 is the thermal conductivity.

$$\rho c_p T_t = -\nabla \cdot (\rho c_p T \mathbf{u} - k_0 \nabla T). \tag{2.12}$$

Applying the chain rule of divergence

$$\rho c_p T_t = -\rho c_p (\nabla T) \cdot \mathbf{u} - \rho c_p (\nabla \cdot \mathbf{u}) T + k_0, \nabla^2 T \tag{2.13}$$

11

and since our fluid is incompressible by (2.7), equation (**??**) reduces to

$$\rho c_p T_t = k_0 \nabla^2 T - \rho c_p (\nabla T) \cdot \mathbf{u}. \tag{2.14}$$

Dividing through by ρc_p and defining the thermal diffusivity constant to be $\alpha = \frac{k_0}{\rho c_p}$ results in

$$T_t = \alpha \nabla^2 T - (\nabla T) \cdot \mathbf{u}. \tag{2.15}$$

By applying (2.6) to (2.15) we may rewrite our conservation of energy equation in the following way.

$$T_t + u T_x + w T_z = \alpha [T_{xx} + T_{zz}]. \tag{2.16}$$

For our model we assume steady-state conditions on our fluid flow however we deal with the transient heat problem. The steady-state condition is represented mathematically as (2.17).

$$\mathbf{u}_t = \mathbf{0} \tag{2.17}$$

We begin our work on the conservation of momentum equation by first writing equation (2.9) as separate equations for each direction of momentum as well as the expanded conservation of mass equation; in this case we have an x-momentum in equation (2.19) and z-momentum in equation (2.23).

$$u_x + w_z = 0, \tag{2.18}$$

$$\rho [uu_x + wu_z] = -p_x + \mu [u_{xx} + u_{zz}], \tag{2.19}$$

$$\rho [uw_x + ww_z] = -p_z + \mu [w_{xx} + w_{zz}]. \tag{2.20}$$

We define our dimensionless variables by scaling them on characteristic values. We scale z on the period of corrugation λ, x on the average annular gap h_0, and the directional velocities u and w on characteristic velocities U and W respectively. Our pressure variable p is scaled on a characteristic pressure P, temperature on the temperature difference $\Delta T := T_{inlet} - T_{ext}$, and time t on the characteristic velocity W over the period of corrugation λ.

$$z^* = \frac{z}{\lambda}; x^* = \frac{x}{h_0}; u^* = \frac{u}{U}; w^* = \frac{w}{W}; p^* = \frac{p}{P}; T^* = \frac{T - T_{ext}}{\Delta T}; t^* = \frac{tW}{\lambda}. \tag{2.21}$$

It should be noted that in this formulation of T^* represents the ratio of the temperature at any point in comparisson to the difference between the inlet and outlet, assuming a minimum value of 0 corresponding to equilibrium with the soil and a maximum value of 1 corresponding to the inlet temperature. We wish to find a relationship between U and W so we apply our conservation of mass equation (2.18) in order to accomplish this and end up with the following relation.

$$\frac{U}{h_0} u_x + \frac{W}{L} w_z \Rightarrow U = \frac{h_0}{\lambda} W. \tag{2.22}$$

Substituting the non-dimensionalized variables into (2.19) and (2.20) we get the non-dimensional form of the conservation of momentum equations.

$$\rho \left[\frac{W^2 h_0}{\lambda^2} u^* u_{x^*}^* + \frac{W^2 h_0}{\lambda^2} w^* u_{z^*}^* \right] = -\frac{P}{h_0} p_{x^*}^* + \mu \left[\frac{W}{\lambda h_0} u_{x^* x^*}^* + \frac{W h_0}{\lambda^3} u_{z^* z^*}^* \right]. \tag{2.23}$$

$$\rho \left[\frac{W^2}{\lambda} u^* w^*_{x^*} + \frac{W^2}{\lambda} w^* w^*_{z^*} \right] = -\frac{P}{\lambda} p^*_{z^*} + \mu \left[\frac{W}{h_0^2} w^*_{x^* x^*} + \frac{W}{\lambda^2} w^*_{z^* z^*} \right]. \tag{2.24}$$

We expect the pressure term to balance the viscous forces within the fluid which allows us to find P in terms of W as outlined below. We work with the z-momentum equation for this.

$$\frac{P}{\lambda} : \frac{\mu W}{h_0^2} \Rightarrow P = \frac{\mu W \lambda}{h_0^2}. \tag{2.25}$$

By rearranging and eliminating terms we are able to reduce our non-dimensionalization to equations (2.29) and (2.30) with two new non-dimensional coefficients to note. We term (2.26) the Reynolds number [7], which represents the ratio of inertial forces to viscous forces within the fluid.

$$\frac{\rho W h_0}{\mu} = \mathbf{Re}. \tag{2.26}$$

The other non-dimensional coefficient is our aspect ratio and serves to facilitate our perturbation expansion which will be treated later in this chapter.

$$\gamma = \frac{h_0}{\lambda}. \tag{2.27}$$

As mentioned earlier in this chapter we look at our problem over two length scales, thus we define a second aspect ratio δ defined below to be used in Chapter 4.

$$\delta = \frac{\lambda}{L}. \tag{2.28}$$

We express the final forms of the non-dimensional x and z momentum equations below. We remove the superscripts (*) in the dependent and independent variables for clarity.

$$\gamma^2 \mathbf{Re} \left[u u_x + w u_z \right] = -p_x + \gamma \left[u_{xx} + \gamma^2 u_{zz} \right]. \tag{2.29}$$

$$\gamma \mathbf{Re} \left[u w_x + w w_z \right] = -p_z + \left[w_{xx} + \gamma^2 w_{zz} \right]. \tag{2.30}$$

By using the same non-dimensional coefficients we arrive at the following representation of our conservation of energy equation.

$$\begin{aligned} &\left[\frac{W}{\lambda} (\Delta T T^* + T_{ext})_{t^*} + \frac{W}{\lambda} u^* (\Delta T T^* + T_{ext})_{x^*} + \frac{W}{\lambda} w^* (\Delta T T^* + T_{ext})_{z^*} \right] \\ = \; &\alpha \left[\frac{1}{h_0^2} (\Delta T T^* + T_{ext})_{x^* x^*} + \frac{1}{\lambda^2} (\Delta T T^* + T_{ext})_{z^* z^*} \right]. \end{aligned} \tag{2.31}$$

Again, we remove the superscripts (*) from our non-dimensionalized variables for clarity and list the non-dimensionalized equations for conservation of momentum and energy below.

$$\frac{W}{\lambda} \left[T_t + u T_x + w T_z \right] = \frac{\alpha}{h_0^2} \left[T_{xx} + \frac{h_0^2}{\lambda^2} T_{zz} \right]. \tag{2.32}$$

By rearranging coefficients we isolate the non-dimensional coefficient called the Péclet number [32]. The Péclet number is defined as the ratio of the rate of advection of a physical quantity by

the flow to the rate of diffusion of the same quantity. By substituting this variable into (2.32) we may obtain the non-dimensionalized conservation of energy equation (2.34) in terms of the Péclet number and our previously defined aspect ratio γ.

$$\mathbf{Pe} = \frac{W h_0}{\alpha}. \tag{2.33}$$

$$\gamma \mathbf{Pe} \left[T_t + u T_x + w T_z \right] = T_{xx} + \gamma^2 T_{zz}. \tag{2.34}$$

Now that we have completed our non-dimensionalization of the conservation of mass, momentum, and energy equations we must non-dimensionalize our boundary conditions before we begin to solve our steady state fluid flow profiles. In order to non-dimensionalize our boundary conditions we first find the normal and tangent of our surface at the corrugated boundary defined at $x = h(z)$. From our dimensional form of $h(z)$ we simply non-dimensionalize it by scaling on h_0. We get the following non-dimensionalized form of $h(z)$.

$$h(z) = 1 + \varepsilon \sin(z) \text{ where } \varepsilon \in [0, 1). \tag{2.35}$$

We take the gradient of our boundary to find the normal and tangent to the boundary as shown in (2.36) and we get expressions for the normal and tangent of our corrugated boundary in (2.37) and (2.38) respectively.

$$\bigtriangledown (x - h(z)) = 0 \tag{2.36}$$

$$\hat{\mathbf{n}} = \frac{\hat{\imath} - h'(z)\hat{k}}{\sqrt{1 + |h'(z)|^2}}. \tag{2.37}$$

$$\hat{\mathbf{t}} = \frac{h'(z)\hat{\imath} + \hat{k}}{\sqrt{1 + |h'(z)|^2}}. \tag{2.38}$$

Using our previously defined scaling terms we non-dimensionalize (2.37) and (2.38) giving us the non-dimensionalized forms of the normal and tangent.

$$\hat{\mathbf{n}} = \frac{\hat{\imath} - \gamma h'(z)\hat{k}}{\sqrt{1 + \gamma^2 h'(z)^2}}. \tag{2.39}$$

$$\hat{\mathbf{t}} = \frac{\gamma h'(z)\hat{\imath} + \hat{k}}{\sqrt{1 + \gamma^2 h'(z)^2}}. \tag{2.40}$$

Since the fluid velocity is assumed to be much less in the radial direction than in the vertical direction we represent $\mathbf{u}$ as

$$\mathbf{u} = \gamma u(x, z)\hat{\imath} + w(x, z)\hat{k}. \tag{2.41}$$

To arrive at expressions for our boundary conditions we solve the following equations at $x = h(z)$. This gives us the relations in equations (2.44) and (2.45).

$$\mathbf{u} \cdot \hat{\mathbf{n}} = 0, \tag{2.42}$$

$$\mathbf{u} \cdot \hat{\mathbf{t}} = 0, \tag{2.43}$$

14

$$u(h(z),z) = w(h(z),z)h'(z), \tag{2.44}$$

$$w(h(z),z) + \gamma^2 u(h(z),z)h'(z) = 0. \tag{2.45}$$

Lastly we non-dimensionalize our gradient operator and our expression for Newton's law of cooling and the no flux condition at the corrugation, given here.

$$\nabla = \frac{1}{h_0}\frac{\partial}{\partial x}\hat{\imath} + \frac{1}{\lambda}\frac{\partial}{\partial z}\hat{k} = \frac{1}{h_0}\left(\frac{\partial}{\partial x}\hat{\imath} + \gamma\frac{\partial}{\partial z}\hat{k}\right). \tag{2.46}$$

$$-k_0 T_x = \eta_0(T_{ext} - T) \quad \text{on} \quad x = 0. \tag{2.47}$$

$$\nabla T \cdot \hat{\mathbf{n}} = 0 \quad \text{on} \quad x = h(z). \tag{2.48}$$

We apply non-dimensionalization and get the following result for our Newton's law of cooling condition.

$$-\frac{k_0}{h_0}(T^*\Delta T)_{x^*} = -\eta_0 T^*\Delta T. \tag{2.49}$$

As ΔT is a constant we can reduce equation (2.49) to

$$\frac{k_0}{h_0}T^*_{x^*} = \eta_0 T^*. \tag{2.50}$$

We define a new non-dimensional constant called the Nusselt number (**Nu**) [32] we get our boundary condition in (2.51). The Nusselt number represents the ratio of heat transfer from the soil to conduction within the fluid. Once again, we drop the superscripts (*) from our equations for clarity, and the nondimensional boundary conditions become

$$T_x = \mathbf{Nu}\,T \quad \text{on} \quad x = 0, \tag{2.51}$$

$$\nabla T \cdot \hat{\mathbf{n}} = 0 \quad \text{on} \quad x = h(z), \tag{2.52}$$

$$\mathbf{Nu} = \frac{\eta_0 h_0}{k_0}. \tag{2.53}$$

For clarity we list all of our relevant equations once again in nondimensional form.

$$u_x + w_z = 0. \tag{2.54}$$

$$\gamma^2 \mathbf{Re}\left[uu_x + wu_z\right] = -p_x + \gamma\left[u_{xx} + \gamma^2 u_{zz}\right]. \tag{2.55}$$

$$\gamma \mathbf{Re}\left[uw_x + ww_z\right] = -p_z + \left[w_{xx} + \gamma^2 w_{zz}\right]. \tag{2.56}$$

$$\gamma \mathbf{Pe}\left[T_t + uT_x + wT_z\right] = T_{xx} + \gamma^2 T_{zz}. \tag{2.57}$$

Boundary Conditions:

$$T_x = \mathbf{Nu}\,T \quad \text{on} \quad x = 0. \tag{2.58}$$

$$\nabla T \cdot \hat{\mathbf{n}} = 0 \quad \text{on} \quad x = h(z). \tag{2.59}$$

$$\mathbf{u} = \mathbf{0} \quad \text{on} \quad x = 0. \tag{2.60}$$

$$\mathbf{u} = \mathbf{0} \quad \text{on} \quad x = h(z). \tag{2.61}$$

Variable	Value
Re	186
Pe	1300
Nu	4
γ	10^{-1} - 10^{-4}
δ	$\times 10^{-4}$

Table 2.1: A list of characteristic values [17]

We provide here the representative values of our dimensionless variables with respect to vertical GHSPs.

Now that we have non-dimensionalized our system and conditions we may proceed by solving for our steady state fluid flow equations. Since there are no known solutions to the Navier-Stokes equations for general Reynolds numbers we must approximate a solution. In the next Chapter we employ a technique known as Perturbation Theory in order to approximate solutions to the fluid flow and heat equations before utilizing a Crank-Nicolson finite difference scheme to numerically approximate a solution to the heat transfer problem.

Chapter 3

Small Annular Limit

There exists a wide range of differential equations which have no known solution, however often it is useful to approximate the behavior of these functions. Perturbation theory provides a collection of methods with which one can perform a systematic analysis to the global behavior of approximations of these solutions [14]. The general idea of this theory is to determine some small scale ($\gamma \ll 1$ in our case) such that as this scale approaches 0 the problem becomes solvable. Once such a parameter is identified all variables are expanded in a power series of this small scale convergent to the original variable as is done in equations (3.1)-(3.4).

With these variables constructed in this manner a system of differential equations can be expanded into a new system for each order of the problem, i.e. $O(1)$, $O(\gamma)$, ... , $O(\gamma^n)$. Since this scale is small it takes relatively few terms to achieve a good approximation as each order problem contains an error of the next order [13]. We expand the dependent variables in an asymptotic expansion in γ

$$u = u_0 + \gamma u_1 + \gamma^2 u_2 + ... \tag{3.1}$$
$$w = w_0 + \gamma w_1 + \gamma^2 w_2 + ... \tag{3.2}$$
$$p = p_0 + \gamma p_1 + \gamma^2 p_2 + ... \tag{3.3}$$
$$T = T_0 + \gamma T_1 + \gamma^2 + ... \tag{3.4}$$

We now proceed to expand our equations to develop a system of equations for each order of γ. As an example of this method, we expand our conservation of mass equation (2.7) below. Such an expansion allows us to establish a relationship between the different order fluid flow equations at each respective order.

$$u_x + w_z = 0 = (u_{0x} + w_{0z}) + \gamma(u_{1x} + w_{1z}) + \gamma^2(u_{2x} + w_{2z}) + ... \tag{3.5}$$

It is a known mathematical result that the set $\{\gamma^n\}$ is linearly independent, thus by the definition of linear independence we have the following result for each order of our expansion.

$$u_{ix} + w_{iz} = 0 \text{ for } i = 0, 1, 2, ..., n \tag{3.6}$$

This expansion in terms of γ is performed on each of our equations (2.51)-(2.61) under the assumption that $\mathbf{Pe} = O(\gamma)$ and $\mathbf{Nu} = O(\gamma^2)$. Utilizing this formulation of the problem we are able to deduce an equation for each order of γ for each of the above equations, listed below.

$O(1)$

$$-p_{0x} = 0. \tag{3.7}$$

$$p_{0z} = w_{oxx}. \tag{3.8}$$

$$T_{0xx} = 0. \tag{3.9}$$

$$T_{0x}(0,z,t) = 0. \tag{3.10}$$

$$T_{0x}(h(z),z,t) = 0. \tag{3.11}$$

Since we are interested in the heat transfer to the fluid in the annular gap, that is comparable to the advection from the leading order fluid flow, we consider only energy conservation for higher orders of γ.

$O(\gamma)$

$$T_{1xx} = 0. \tag{3.12}$$

$$T_{1x}(0,z,t) = 0. \tag{3.13}$$

$$T_{1x}(h(z),z,t) = 0. \tag{3.14}$$

$O(\gamma^2)$

$$T_{2xx} = \overline{\mathbf{Pe}}[T_{0t} + u_0 T_{0x} + w_0 T_{0z}] - T_{0zz}. \tag{3.15}$$

$$T_{2x}(0,z) = \overline{\mathbf{Nu}}T_0. \tag{3.16}$$

$$T_{2x} - h'(z)T_{0z} = 0. \tag{3.17}$$

Now that we have established the corresponding equations for every order of γ we wish to solve the leading-order problem for the conservation of momentum equations (3.7) and (3.8). This gives us the system of equations related to $O(1)$ fluid flow. From (3.7) it is clear that p_0 is only a function of z: $p_0 = p_0(z)$. We antidifferentiate (3.8) with respect to x and arrive at the following function.

$$w_0 = \frac{x^2 p_{0z}(z)}{2} + Ax + B. \tag{3.18}$$

We use our boundary conditions at $O(1)$ in equations (2.60) and (2.61) to solve for A and B and arrive at the equation for w_0 in terms of the pressure gradient given in (3.19)

$$w_0 = \frac{x p_{0z}(z)}{2}(x - h(z)). \tag{3.19}$$

Now that we have an expression for w_0 in terms of p_{0z} we use the conservation of mass equation (3.6) to find an expression for u_0.

$$u_0 = \frac{x^2 h(z) p_{0zz}(z)}{4} + \frac{x^2 h'(z) p_{0z}(z)}{4} - \frac{x^3 p_{0zz}(z)}{6} + C. \tag{3.20}$$

Our boundary conditions for u_0 are identical to the conditions we have for w_0 thus we determine $C = 0$. At $u_0(h(z), z)$ we have the following relation.

$$u_0(h(z), z) = \frac{h^3(z) p_{0zz}}{12} + \frac{h^2(z) h'(z) p_{0z}}{4} = 0. \tag{3.21}$$

We simplify this equation by taking advantage of the fact that our equation is overdetermined and we solve directly for the pressure gradient, given in (3.23). The pressure gradient is negative simply because fluid flows from high pressure to low pressure.

$$u_0(h(z), z) = \frac{\partial}{\partial z}(h^3(z) p_{0z}) = 0. \tag{3.22}$$

$$p_{0z} = \frac{-1}{h^3(z)}. \tag{3.23}$$

We now have our expression for the $O(1)$ pressure term, and we substitute this into equations (3.20) and (3.18) to arrive at equations (3.24) and (3.25) for our leading order fluid flow.

$$w_0 = \frac{x}{2h^2(z)} \left(1 - \frac{x}{h(z)}\right). \tag{3.24}$$

$$u_0 = \frac{x^2 h'(z)}{2h^3(z)} \left(1 - \frac{x}{h(z)}\right). \tag{3.25}$$

We next solve the conservation of energy equation given in equation (3.9) under the previously asserted assumptions that $\mathbf{Pe} = O(\gamma)$ and $\mathbf{Nu} = O(\gamma^2)$. Our $O(1)$ case is very straightforward; the resulting equation (3.9), solved in conjunction with its boundary conditions given in equations (3.10) and (3.11) gives us simply that T_0 is independent of x as shown in equation (3.26).

$$T_0 = T_0(z, t). \tag{3.26}$$

This same relation holds true for the $O(\gamma)$ case given in equation (3.12), so we move to the $O(\gamma^2)$ case. For clarity we outline the solution to the $O(\gamma)$ problem.

$$T_1 = T_1(z, t). \tag{3.27}$$

We solve for the $O(\gamma^2)$ conservation of energy equation given in equation (3.15) in the same manner.

Simplifying (3.17) gives us the following relation between T_{2x} and T_0 .

$$T_{2x} - h'(z) T_{0z} = 0 \text{ at } x = h(z). \tag{3.28}$$

We substitute our w_0 fluid flow equation (3.24) into (3.15) and integreate with respect to x to achieve equation (3.29). Notice the T_{0x} term is removed as we have established T_0 is independent of x.

$$T_{2x}(h(z), z, t) - T_{2x}(0, z, t) = \overline{\mathbf{Pe}} \left[h(z) T_{0t} + \frac{1}{12} T_{0z}\right] - h(z) T_{0zz}. \tag{3.29}$$

19

By substituting our relation between T_{0z} and $T_{2x}(h(z), z, t)$ given in (3.17) into equation (3.29) we arrive at the final expression (3.30) for the temperature within our system.

$$\overline{\mathbf{Pe}} \left[h(z) T_{0t} + \frac{1}{12} T_{0z} \right] - [h(z) T_{0z}]_z = -\overline{\mathbf{Nu}} T_0. \tag{3.30}$$

3.1 Crank-Nicolson Results

Since there does not exist any analytical solution to equation (3.30) the solution required an approximation scheme. We utilized a Crank-Nicolson scheme as outlined in Appendix B.3 to approximate these values at each time step. Due to the advective term we utilize an upwinding scheme as outlined in Appendix B.6. Additionally, the incorporation of the boundary $h(z) = 1 + \varepsilon \sin(z)$ into equation (3.30) requires amendments to some of the coefficient matrices. As an example the term $h'(z) T_{0z}$ is approximated as

$$h'(z) T_{0z} \approx h_i' \frac{T_i^j - T_{i-1}^j}{\delta z}. \tag{3.31}$$

When written in matrix form equation (3.31) requires that the upwinding coefficient matrix have the ith row multiplied by $h(z_i)$ for each i. Similarly the diffusion coefficient matrix and time dependent identity matrix also must be modified in this same manner.

With this formulation of the Crank-Nicolson method we proceeded to analyze our results for the solution of (3.30). We began by plotting the transient propagation for various ε and $\overline{\mathbf{Pe}}$. The specific time steps plotted are not the same for each set of parameters but rather represent an even partition from the initial condition to the steady state. In all of the cases plotted the propagation approaches the same temperature profile independent of the corrugation amplitude ε.

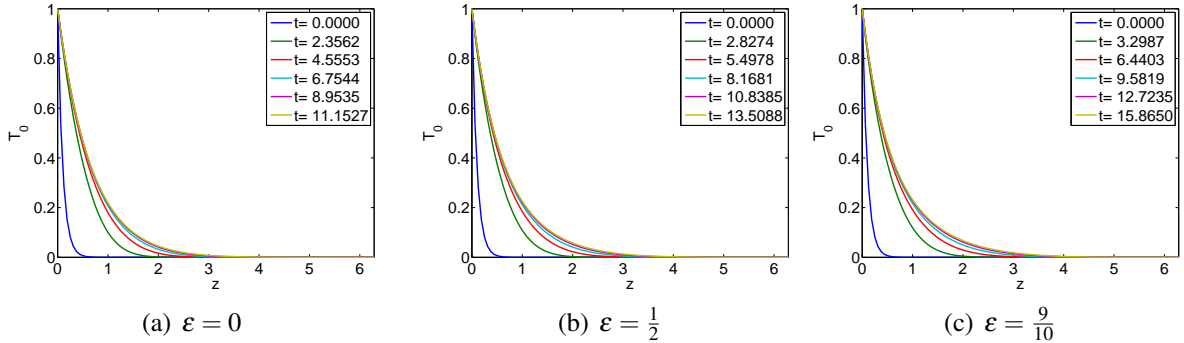(a) $\varepsilon = 0$ (b) $\varepsilon = \frac{1}{2}$ (c) $\varepsilon = \frac{9}{10}$

Figure 3.1: Temperature over time for equation 3.30 for various corrugation amplitudes ε. Time steps are evenly spaced from the initial condition to the steady-state profile for $T_0(z,0) = e^{-10z}$, $\overline{\mathbf{Pe}} = 13$ and 1 corrugation period.

(a) $\varepsilon = 0$ (b) $\varepsilon = \frac{1}{2}$ (c) $\varepsilon = \frac{9}{10}$

Figure 3.2: Temperature plotted over time for equation 3.30 for various corrugation amplitudes ε. Time steps are evenly spaced from the initial condition to the steady-state profile for $T_0(z,0) = e^{-10z}$, $\overline{\mathbf{Pe}} = 130$ and 10 corrugation period.
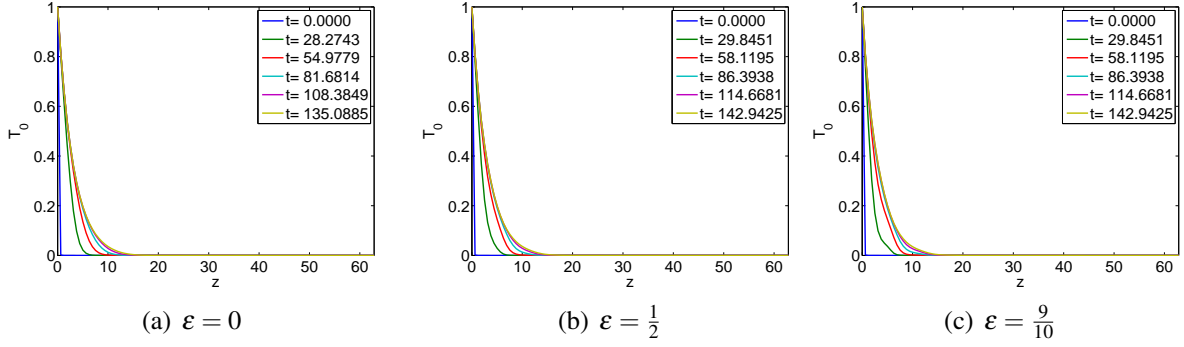

(a) $\varepsilon = 0$ (b) $\varepsilon = \frac{1}{2}$ (c) $\varepsilon = \frac{9}{10}$
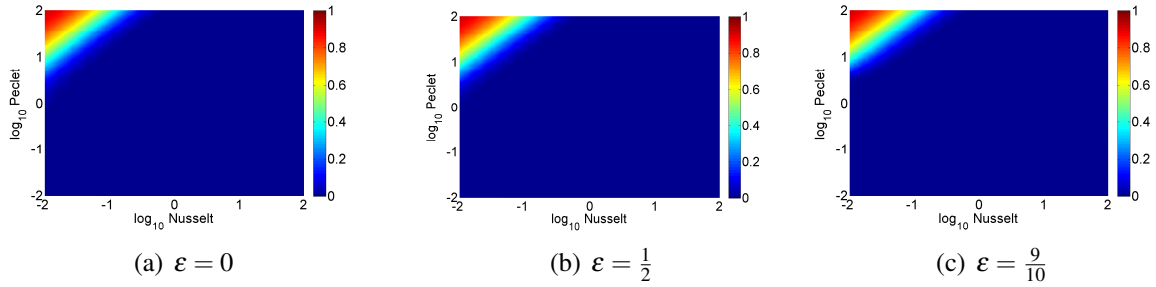
Figure 3.3: Steady State Temperature of (3.30) over 10 corrugations

We run our Crank-Nicolson algorithm until the relative error between any two consecutive time steps is less than 10^{-8}. As can be seen in the graphs in Figure 3.3 the steady state solutions are independent of epsilon. It is also worth noting that for all $\mathbf{Nu} \geq \frac{\mathbf{Pe}}{100}$ complete thermal equilibrium with the soil is accomplished, while for large $\mathbf{Pe}$ values the advection dominates the transfer and little or no thermal transfer between the fluid and soil occurs. From all of these solutions we are able to determine that the corrugation has no effect on the steady state temperature under the assumption of low $\mathbf{Re}$.

In this chapter we have been able to approximate the transient temperature profile within an annular gap under the constraints of a low $\mathbf{Re}$ and small annular gap. As we expanded the number of corrugations in this pipe we determined that the steady-state temperature profile is independent of the corrugation amplitude ε. As the steady-state profile within this model becomes uniform in ε over these several periods we create a second model based on a homogenization approach in addition to a simulation to determine whether these results hold true over the length of the entire pipe.

Chapter 4

Full Bore-Hole Limit

We want to look at the behavior of the heat transfer over not just one period of our pipe ($L = 2\pi$) but over several periods ($L = 2n\pi : n \in \mathbb{N}$). Here it is assumed that the number of periods is relatively large, i.e. $n \geq O(10^3)$. In order to approach this formulation we begin by introducing a large scale $\zeta = \delta z$ where $\delta = \frac{\lambda}{L}$ (length of corrugation period/length of pipe). For an idea of these length scales refer to Figure 4.1(a). With this new formulation we can proceed to solve this process using a Homogenization method. For a detailed explanation of the method of Homogenization refer to [58]. It is important to note that in this formulation $\gamma = O(1)$.

Equation (4.1) now has components which operate on both a macro-scale and a micro-scale. In proceeding with this formulation it is assumed that the temperature propagation on this macro-scale is independent of the micro-scale. It is of note that we now have no restrictions on the values which **Pe** can assume, so we assume that **Pe** $= O(1)$ and **Nu** $= O(\delta)$ while maintaining the low **Re** close to 0.

$$\mathbf{Pe}\,\mathbf{u}\,\bigtriangledown T - \bigtriangledown^2 T = 0. \tag{4.1}$$

Incorporating this new scale into our linear operators from equation (4.1) they expand to

$$\bigtriangledown T = T_x \hat{\imath} + (T_z + \delta T_\zeta)\hat{k}, \tag{4.2}$$

and

$$\bigtriangledown^2 T = T_{xx} + (T_{zz} + 2\delta T_{z\zeta} + \delta^2 T_{\zeta\zeta}). \tag{4.3}$$
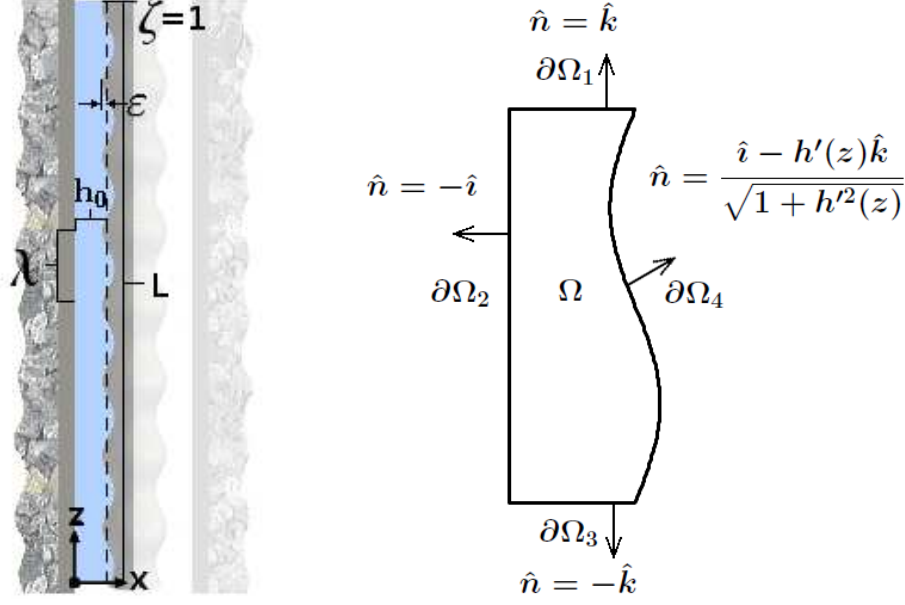
(a) $\zeta = 1$ corresponds to the length of the whole pipe

(b) Micro-Scale Boundary Ω

Figure 4.1: Homogenization Scales

We shall define the rest of our variables as in the asymptotic problem seen in Chapters 2 and 3 excepting the perturbation is done with respect to δ. Similarly we define the fluid velocity profile to be of the form

$$\mathbf{u} = u(x,z)\hat{\imath} + w(x,z)\hat{k}. \tag{4.4}$$

The non-dimensionalized temperature T is expanded in powers of δ as

$$T(x,z,\zeta) = T_0 + \delta T_1 + \delta T_2 + ... \tag{4.5}$$

Our micro-scale is defined as in Figure 4.1(b) and due to the independence of ζ and z we force periodicity in z, rendering the boundary conditions

$$\begin{array}{llll} \triangledown T \cdot \hat{\imath} &=& -\delta\, \mathbf{Nu}\, T & \text{on } x = 0; \quad \triangledown T(x,0,\zeta) = \triangledown T(x,2\pi,\zeta); \\ \triangledown T \cdot \hat{\mathbf{n}} &=& 0 & \text{on } x = h(z); \quad T(x,0,\zeta) = T(x,2\pi,\zeta). \end{array} \tag{4.6}$$

Our leading order problem becomes

$$\mathbf{Pe}\,[u_0 T_{0x} + w_0 T_{0z}] - T_{0xx} - T_{0zz} = 0, \tag{4.7}$$

subject to the boundary conditions

$$\begin{array}{llll} \triangledown T_0 \cdot \hat{\imath} &=& 0 & \text{on } x = 0; \quad \triangledown T_0(x,0,\zeta) = \triangledown T_0(x,2\pi,\zeta); \\ \triangledown T_0 \cdot \hat{\mathbf{n}} &=& 0 & \text{on } x = h(z); \quad T_0(x,0,\zeta) = T_0(x,2\pi,\zeta). \end{array} \tag{4.8}$$

The only solution which satisfies (4.7) is that T_0 is a function of ζ alone as ζ belongs to the null space of the linear operator, thus we have $T_0(\zeta)$.

23

At $O(\delta)$ a relation between T_1 and T_0 can be found by utilizing the expansion of the gradient and Laplacian operators given in equations (4.2) and (4.3).

$$\mathbf{Pe}\left[u_0 T_{1x} + w_0 T_{1z}\right] - T_{1xx} - T_{1zz} = -\mathbf{Pe}\,w_0 T_{0\zeta} + T_{0z\zeta}. \tag{4.9}$$

Since T_0 is independent of z, $T_{0z\zeta} = 0$, and equation (4.9) can be expressed as in equation (4.10)

$$\mathbf{Pe}\left[u_0 T_{1x} + w_0 T_{1z}\right] - T_{1xx} + T_{1zz} = -\mathbf{Pe}\,w_0 T_{0\zeta}, \tag{4.10}$$

subject to the boundary conditions

$$
\begin{aligned}
\triangledown T_1(h(z),z,\zeta)\cdot\hat{\mathbf{n}} &= 0; & \triangledown T_1(x,0,\zeta) &= \triangledown T_1(x,2\pi,\zeta); \\
T_{1x}(0,z,\zeta) &= -\mathbf{Nu}\,T_0; & T_1(x,0,\zeta) &= T_1(x,2\pi,\zeta).
\end{aligned} \tag{4.11}
$$

In equation (4.10) T_1 is defined on $\Omega = [0,2\pi] \times [0,h(z)]$ as displayed in Figure 4.1(b). We now define the linear operator $\mathscr{L} : \Omega \mapsto \mathbb{R}$ defined by

$$\mathscr{L} = \mathbf{Pe}\,\mathbf{u}\cdot\triangledown - \triangledown^2, \tag{4.12}$$

where the gradient and divergence operators are independent of ζ due to the domain. To prove the existence of solutions to the higher order problems we turn to the Fredholm alternative theorem, given below.

Fredholm Alternative Theorem 1. *Let $\mathscr{L}$ be a bounded linear operator in a Hilbert space H with closed range R. There exists a solution to $\mathscr{L}(T) = f$ iff $< f,g >= 0$ for all g s.t. $\mathscr{L}^\dagger(g) = 0$. [59]*

Similar versions of this theorem with respect to linear operators in Hilbert and Banach spaces, as well as for linear algebra may be found in [51] and [50]. In order to solve the adjoint criterion of this problem we first define an inner product on the space to be the L^2 norm for any two scalar functions in our Hilbert space Ω as

$$< \theta,\phi >= \iint_\Omega \theta\phi\,dV. \tag{4.13}$$

We now attempt to find the adjoint $\mathscr{L}^\dagger$ of $\mathscr{L}$ by imparting the boundary conditions in equation (4.8) on θ.

$$< \mathscr{L}(\theta),\phi >=< \theta,\mathscr{L}^\dagger(\phi) >= 0. \tag{4.14}$$

Since θ and ϕ are scalar functions, then $(\theta\,\mathbf{u}\,\phi)$ is a vector and we can utilize Green's theorem.

$$\iint_\Omega \triangledown\cdot(\theta\,\mathbf{u}\,\phi)\,dV = \oint_{\partial\Omega} \theta\phi(\mathbf{u}\cdot\hat{\mathbf{n}})\,dS, \tag{4.15}$$

$$\triangledown\cdot(\theta\,\mathbf{u}\,\phi) = \phi\,\mathbf{u}\cdot\triangledown\theta + \theta\,\mathbf{u}\cdot\triangledown\phi + \theta\phi\,\triangledown\cdot\mathbf{u}. \tag{4.16}$$

Based on the conservation of mass equation we know that $\triangledown\cdot\mathbf{u} = 0$ and thus the two following relations hold.

$$\nabla \cdot (\theta \, \mathbf{u}) = \mathbf{u} \cdot \nabla \theta + \theta \nabla \cdot \mathbf{u} = \mathbf{u} \cdot \nabla \theta, \tag{4.17}$$

$$\nabla \cdot (\phi \theta \, \mathbf{u}) = \phi \, \mathbf{u} \cdot \nabla \theta + \theta \, \mathbf{u} \cdot \nabla \phi = \phi \nabla \cdot (\theta \, \mathbf{u}) + \theta \, \mathbf{u} \cdot \nabla \phi. \tag{4.18}$$

Combining these equations we arrive at

$$\iint_{\Omega} \phi \nabla \cdot (\theta \, \mathbf{u}) dV = \oint_{\partial \Omega} \theta \phi (\mathbf{u} \cdot \hat{\mathbf{n}}) dS - \iint_{\Omega} \theta \, \mathbf{u} \cdot \nabla (\phi) dV. \tag{4.19}$$

The implication of this being that if

$$\oint_{\partial \Omega} \theta \phi (\mathbf{u} \cdot \hat{\mathbf{n}}) dS = 0, \tag{4.20}$$

then the linear operator $\mathscr{S} = \mathbf{u} \cdot \nabla$ has adjoint operator $\mathscr{S}^{\dagger} = -\mathbf{u} \cdot \nabla$. Expanding this procedure to the Laplacian operator $\mathscr{T} = \nabla^2$ we have that

$$< \mathscr{T}(\theta), \phi > = \iint_{\Omega} \phi \nabla^2 \theta dV. \tag{4.21}$$

Letting $\mathbf{v} = \nabla \theta$ and substituting into equation (4.21) we have

$$\iint_{\Omega} \phi \nabla \cdot \mathbf{v} dV = \iint_{\Omega} \nabla \cdot (\phi \mathbf{v}) dV - \iint_{\Omega} \mathbf{v} \cdot (\nabla \phi) dV. \tag{4.22}$$

Again, utilizing Green's theorem we find that

$$\iint_{\Omega} \phi \nabla \cdot \mathbf{v} dV = \oint_{\partial \Omega} \phi (\mathbf{v} \cdot \hat{\mathbf{n}}) dS - \iint_{\Omega} \mathbf{v} \cdot \nabla \phi dV = \oint_{\partial \Omega} \phi (\mathbf{v} \cdot \hat{\mathbf{n}}) dS - \iint_{\Omega} (\nabla \theta) \cdot (\nabla \phi) dV \tag{4.23}$$

$$\Rightarrow$$

$$\iint_{\Omega} (\nabla \theta) \cdot (\nabla \phi) dV = \iint_{\Omega} \nabla \cdot (\theta \nabla \phi) dV - \iint_{\Omega} \theta \nabla^2 \phi dV = \oint_{\partial \Omega} \theta (\nabla \phi \cdot \hat{\mathbf{n}}) ds - \iint_{\Omega} \theta \nabla^2 \phi dV$$

$$\Rightarrow$$

$$\iint_{\Omega} \phi \nabla^2 \theta dV = \oint_{\partial \Omega} \phi (\nabla \theta \cdot \hat{\mathbf{n}}) dS - \oint_{\partial \Omega} \theta (\nabla \phi \cdot \hat{\mathbf{n}}) ds + \iint_{\Omega} \theta \nabla^2 \phi dV.$$

$$\oint_{\partial \Omega} \phi (\nabla \theta \cdot \hat{\mathbf{n}}) dS - \oint_{\partial \Omega} \theta (\nabla \phi \cdot \hat{\mathbf{n}}) dS = 0. \tag{4.24}$$

Therefore, if the conditions in equation (4.24) hold true then the Laplacian operator ∇^2 is self adjoint. If the conditions in equations (4.20) and (4.24) are satisfied, then our equation reduces down to

$$< \mathscr{L}(\theta), \phi > = \iint_{\Omega} \left(\phi \, \mathbf{u} \cdot \nabla \theta - \phi \nabla^2 \theta \right) dV = \iint_{\Omega} (-\theta \, \mathbf{u} \cdot \nabla \phi - \theta \nabla^2 \phi) dV = < \theta, \mathscr{L}^{\dagger}(\phi) > . \tag{4.25}$$

There are several different boundary conditions which can satisfy the adjoint criterion. We impose the following periodic boundary conditions in the vertical direction and no flux conditions in the axial direction. These are outlined as given below

$$\phi(x,0) = \phi(x,2n\pi), \tag{4.26}$$

$$\bigtriangledown\phi(h(z),z)\cdot\hat{\mathbf{n}} = 0, \tag{4.27}$$

$$\bigtriangledown\phi(0,z)\cdot\hat{\mathbf{n}} = 0, \tag{4.28}$$

$$\bigtriangledown\phi(x,0)\cdot\hat{\mathbf{n}} = \bigtriangledown\phi(x,2n\pi)\cdot\hat{\mathbf{n}}. \tag{4.29}$$

Therefore any constant function satisfies $\mathscr{L}^\dagger(\phi)$ and for simplicity we define $\phi := 1$. Applying this orthogonality constraint to $\mathscr{L}(T_1)$ we have from equation (4.10).

$$< \mathscr{L}(T_1),1 >= -\iint_\Omega \mathbf{Pe}\,w_o T_{0\zeta}dV. \tag{4.30}$$

In order to solve this particular integral we apply the Divergence Theorem and our boundary conditions on T_1, given in equation (4.11). The integral may be rewritten in the form given in equation (4.31) as we have conservation of mass and $\mathbf{Pe}$ is a scalar.

$$-\iint_\Omega \mathbf{Pe}\,w_o T_{0\zeta}dV = \iint_\Omega \bigtriangledown\cdot(\mathbf{Pe\,u}\,T_1 - \bigtriangledown T_1)\,dV. \tag{4.31}$$

With equation (4.31) written in this form we apply the Divergence Theorem.

$$\iint_\Omega \bigtriangledown\cdot[\mathbf{Pe\,u}\,T_1 - \bigtriangledown T_1]\,\mathrm{d}V = \oint_{\partial\Omega}[\mathbf{Pe\,u}\,T_1 - \bigtriangledown T_1]\cdot\hat{\mathbf{n}}dS. \tag{4.32}$$

Defining our boundaries as in Figure 4.1(b) we have the components of this integral on each boundary.

$$\partial\Omega_1 : \oint_0^{h(z)}(\mathbf{Pe\,u}\,T_1 - \bigtriangledown T_1)\cdot\hat{\mathbf{k}}dx, \tag{4.33}$$

$$\partial\Omega_2 : -\oint_0^{2\pi}(\mathbf{Pe\,u}\,T_1 - \bigtriangledown T_1)\cdot\hat{\imath}dz, \tag{4.34}$$

$$\partial\Omega_3 : -\oint_0^{h(z)}(\mathbf{Pe\,u}\,T_1 - \bigtriangledown T_1)\cdot\hat{\mathbf{k}}dx, \tag{4.35}$$

$$\partial\Omega_4 : \oint_{\partial\Omega_4}(\mathbf{Pe\,u}\,T_1 - \bigtriangledown T_1)\cdot\left(\frac{\hat{\imath}-h'(z)\hat{k}}{\sqrt{1+h'(z)^2}}\right)dS. \tag{4.36}$$

We have that $\mathbf{u}=\mathbf{0}$ on $\partial\Omega_2$ and $\partial\Omega_4$, so the first terms are 0 in both equations (4.34) and (4.36). By the no-flux boundary condition on Ω_4 the flux term is 0. By the periodicity in z the terms in equations (4.33) and (4.35) are equal but of opposite sign and thus reduce to 0. Now our order δ equation reduces to

$$-\iint_\Omega \mathbf{Pe}\, w_o T_{0\zeta}\, dV = -\oint_{\partial\Omega_2} \triangledown T_1 \cdot \hat{\mathbf{n}}\, dS = \int_0^{2\pi} \triangledown T_1 \cdot \hat{\imath}\, dz = \int_0^{2\pi} \mathbf{Nu}\, T_0 dz. \tag{4.37}$$

$$-\int_0^{2\pi}\int_0^{h(z)} \mathbf{Pe}\, w_o T_{0\zeta}\, dx\, dz = -\int_0^{2\pi}\int_0^{h(z)} \left(\frac{x}{2h^2(z)}\left(1-\frac{x}{h(z)}\right)\right)\mathbf{Pe}\, T_{0\zeta}\, dx\, dz. \tag{4.38}$$

$$-\int_0^{2\pi}\frac{1}{12}\mathbf{Pe}\, T_{0\zeta} = -\frac{2\pi}{12}\mathbf{Pe}\, T_{0\zeta} = 2\pi\,\mathbf{Nu}\, T_0 \Rightarrow T_0 = e^{\frac{-12\,\mathbf{Nu}}{\mathbf{Pe}}\zeta}.$$

Similarly we can define w_0 in equation (4.37) to be the vertical component of any laminar flow. In this manner we can then express the solution to this equation as

$$T_0 = e^{-\frac{\mathbf{Nu}}{\overline{w_0}\,\mathbf{Pe}}\zeta}. \tag{4.39}$$

where $\overline{w_0}$ is the average vertical flow over the period of corrugation. In this manner this solution to the homogenization can be compared more easily with simulations in which this average velocity is known.

To see how the two different approaches compare we create a $\log_{10}$ relative error plot between our homogenization solution and the perturbation expansion. We create these plots for various ε using the same $\log_{10} \mathbf{Pe}$ and $\mathbf{Nu}$ numbers as before on a boundary of 10 periods of corrugation. As can be seen in Figure 4.2 we find agreement between these two models with our worst error $O(10^{-3})$ which occurs for $\mathbf{Pe} \geq \mathbf{Nu}$.

(a) $\varepsilon = 0$ (b) $\varepsilon = \frac{1}{2}$ (c) $\varepsilon = \frac{9}{10}$
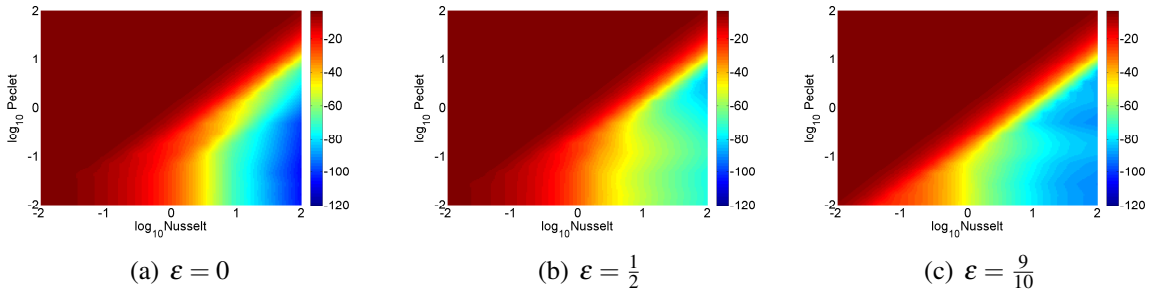
Figure 4.2: $\log_{10}$ Absolute Error of Homogenization vs Crank-Nicolson

To further validate these models we simulate the heat transfer using the COMSOL 4.2a multiphysics platform. We begin our work with COMSOL by importing a specified geometry built in AutoCAD utilizing the sine draw plug-in application and saved in an importable .dwf format. Once we import our boundary we create a linear interpolation along the curve in order to expedite calculation. This geometry is pictured below in Figure 4.3 and the full geometry is 10 periods in length. It is important to note that our work with COMSOL is done with dimensions rather than in a dimensionless frame.

To proceed with our simulation we choose our materials; water, PVC, and soil; as well as our physics packages. We use the Laminar Flow package in addition to the Heat Transfer in Fluids
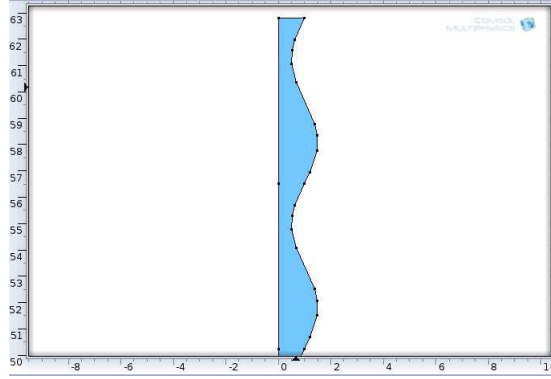
Figure 4.3: COMSOL Geometry

package. We properly assign our materials to their respective boundaries and domains as well as define our initial conditions and boundary conditions identical to the dimensional problem described in Chapter 1. For our heat flux with the soil we derive our heat transfer coefficient from our chosen **Nu** number. For our fluid flow conditions we determine the average fluid velocities corresponding to our chosen values of the **Pe** number. This process becomes necessary as this platform is not capable of handling non-dimensionalized systems with ease. We define a temperature difference of 1 Kelvin between our heat source at the bottom of the pipe ($z = 0$) and the initial fluid and soil temperatures at 298.15 Kelvin. Simulations are then run utilizing the PARDISO solver for various **Re** keeping our conditions unchanged. During this process we utilize a "finer" mesh grid. We show in Figure 4.4 the heat dispersion in the pipe corresponding to a **Re** = 75 as well as the velocity profiles given by the contours over two time periods.

(a) COMSOL **Re** = 75 at time $t = 400s$ (b) COMSOL **Re** = 75 at time $t = 2000s$
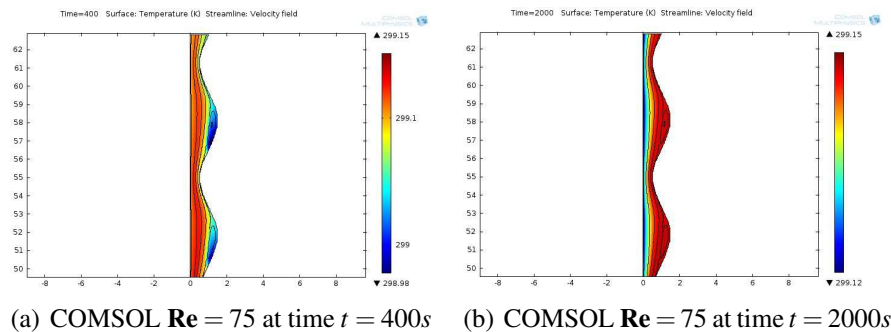
Figure 4.4: Temperature profile and streamlines for last 2 corrugation periods **Re** = 75.

We see clearly that a recirculation occurs where the annular gap is largest even for very low **Re** numbers such as 75. It is important to note that the corrugations "trap" the heat in these eddies however they do not have a significant impact on the overall heat transfer within the pipe over 10 corrugation periods under our assumption of no thermal flux at the corrugation.

In addition to looking at temperature distribution over periods of time we vary the **Re** from 1.86 (**Pe** $\approx$ 13) to 2000 (**Pe** $\approx$ 14000). Note that the finest mesh is used for **Re** < 215 and the coarsest

for **Re** > 2000 while intermediate values require intermediate mesh refinements. In Figure 4.5 we show the steady-state temperature profiles along with the respective velocity contours for several values of **Re** numbers.

(a) Temperature: **Re** = 1.86   (b) Temperature: **Re** = 18.6   (c) Temperature: **Re** = 1250

(d) Velocity: **Re** = 1.86   (e) Velocity: **Re** = 18.6   (f) Velocity: **Re** = 1250
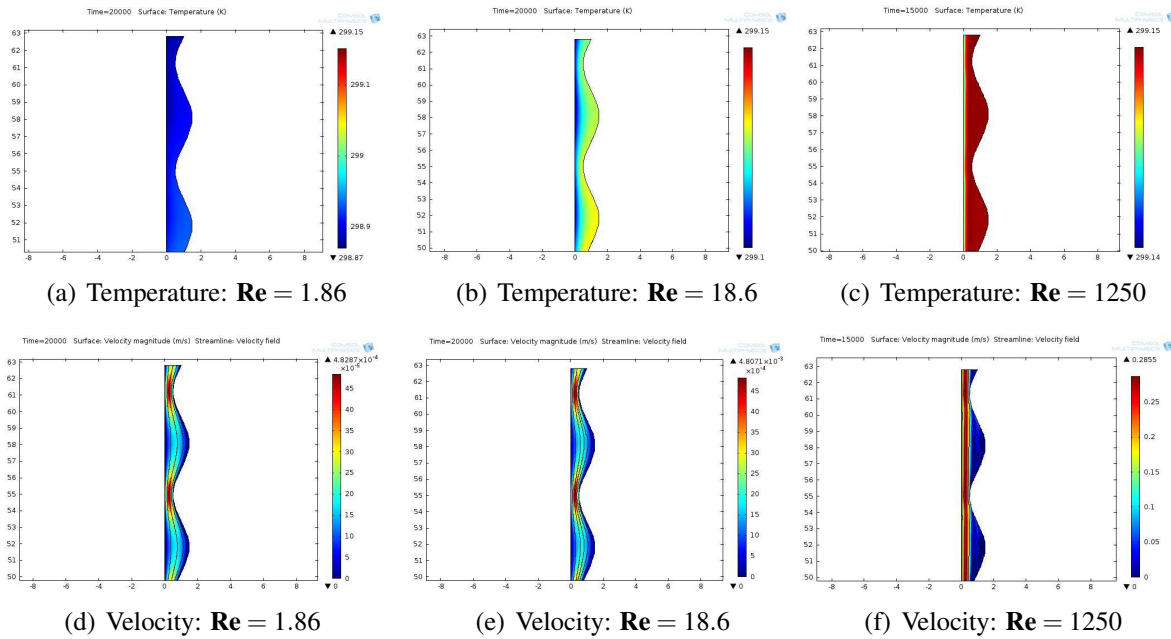
Figure 4.5: COMSOL steady-state temperature and velocity profiles over 10 corrugation periods.

We compare the COMSOL simulations with the steady-state solution from equation 4.39 shown in Figures 4.6 and 4.7 for 10 corrugation periods. The temperature is taken as the averge of the temperature at the end of the pipe calculated in the same manner as shown in Figure 4.5. It should be noted that our Homogenization solution is in terms of temperature difference. For this reason it was required to simply add the inlet temperature (298.15 Kelvin) to the homogenization solutions, as the COMSOL simulation utilized a temperature difference of 1 Kelvin. As can be seen from these plots the simulation approaches the Homogenization solution more rapidly for larger **Pe**. Additionally $\log_{10}$ relative error displays the close agreement between our homogenization solution and the COMSOL simulation.

29

(a) Transient COMSOL vs Homogenization Steady State

(b) $\log_{10}$ Relative Error
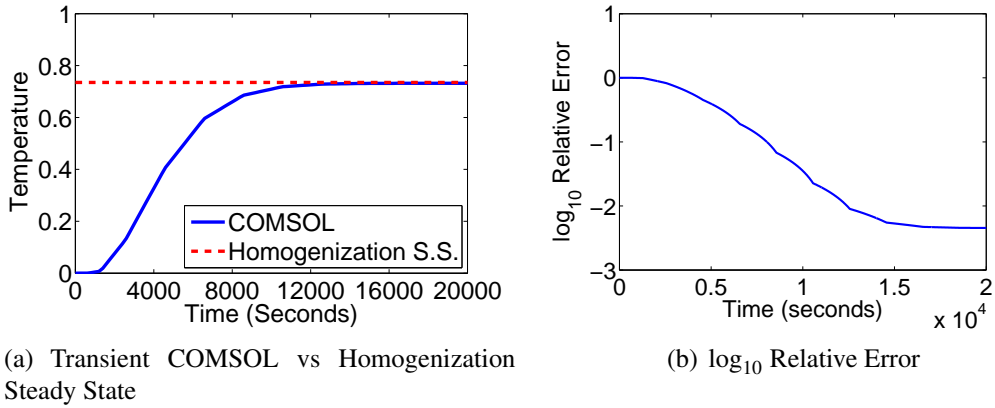
Figure 4.6: Homogenization vs COMSOL $\varepsilon = 0.5$, $\mathbf{Pe} = 13$

(a) Transient COMSOL vs Homogenization Steady State

(b) $\log_{10}$ Relative Error
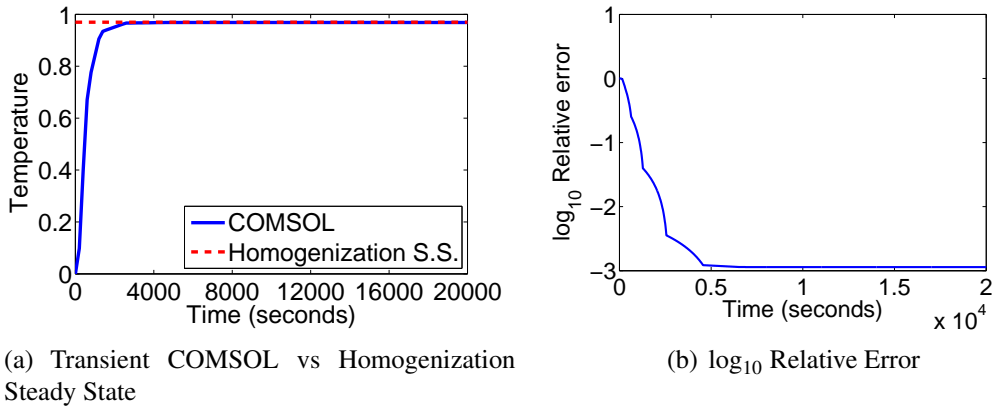
Figure 4.7: Homogenization vs COMSOL, $\varepsilon = 0.5$, $\mathbf{Pe} = 130$

As the system we modeled had the assumption that $\mathbf{Re}$ is close to zero we wish to see how it compares with COMSOL simulations for larger $\mathbf{Re}$. Within COMSOL the larger these values of $\mathbf{Re}$ become, the mesh must be made coarser else the platform returns errors concerning the convergence of a solution for the steady-state fluid flow. For this reason the comparison graph shown in Figure 4.8 displays both the $\mathbf{Re}$ used within the simulation as well as the mesh on which it was solved. The resulting graph displays how even at much higher numbers this homogenization modeling remains consistent with the COMSOL simulation. This similarity between these plots suggests that this model can be used outside of the constraints on the $\mathbf{Re}$ to provide an accurate approximation of the thermal transfer within this concentric system provided the boundary condition assumptions hold.

Figure 4.8: Plot of Temperature at end of pipe (L) for Homogenization and COMSOL models for various **Re**.

Chapter 5

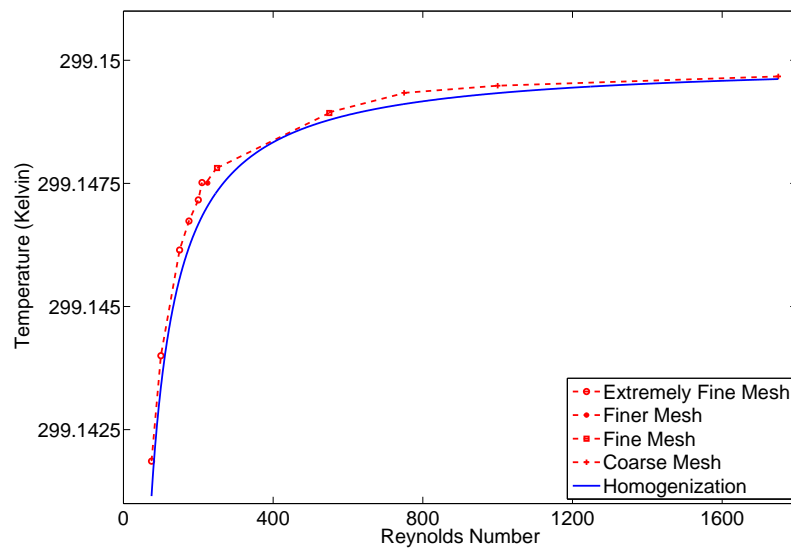# Conclusions

In this project we have studied the effect of a corrugation on the inner return wall of a vertical concentric GSHP with perfect insulation between the core and return pipes. This system is modeled using two different length scales; one period of corrugation as well as over the entire length of the pipe. Non-dimensionalization techniques are utilized to identify the dominant processes within our system. As there are no known solutions to the Navier-Stokes equation for generalized Reynolds numbers, we utilize a perturbation expansion in order to approximate solutions to our fluid flow and heat transfer equations. After solving these systems of equations we developed a Crank-Nicolson scheme with upwinding to numerically solve the temperature profile within a single period of corrugation, as well as over several periods.

While the corrugation had a significant effect on the heat transfer over a single period of corrugation this effect diminished rapidly over additional periods of corrugation. We conclude from this result that for laminar flow profiles corrugation has little to no effect on the heat transfer within this system under the current assumptions.

We then applied the technique of homogenization in space under steady-state conditions to determine the effect of corrugation over the entire length of the pipe and confirm our findings from the Crank-Nicolson result. Our analytical solution to the homogenization problem was independent of the corrugation which agrees with our numerical results obtained by the Crank-Nicolson scheme. In order to validate our methods and their respective results we utilized the COMSOL multiphysics platform to formulate and solve our system over 10 periods of corrugation and compared these results to the homogenization solution. The results obtained from the COMSOL simulation validated our models under the assumption of laminar flow profiles.

Finally we used COMSOL to determine the range of Reynolds numbers for which our models remain valid. This comparison showed that our homogenization model indeed remains relatively accurate for a range of Reynolds numbers from 1 to 2000. We failed to determine a specific Reynolds number at which this homogenization fails to accurately predict the temperature at the end of the pipe, which further validates this model outside the assumption of Reynolds numbers close to zero. This can be seen as the Péclet number, which corresponds to the only dependence on fluid velocity in this equation, is simply the Prandtl number, a constant, multiplied by the Reynolds number. This relation explains the physical independence of our solution from the average fluid velocity.

The assumption of a no-flux boundary condition between the core and return pipe was validated in a smooth pipe by the REU team, however this relation was not analyzed throughout our work and may indeed no longer be valid. By relaxing this to allow a heat flux between the inner pipe and the return pipe we may see an impact on the heat transfer.

In conclusion, our most important result from this work has been in determining that the steady state temperature profile within this system is independent of the corrugation amplitude. While such a result is not beneficial to the improvement of these systems, it is certainly an interesting result which works to further validate the current modeling techniques for these systems.

Appendix A

Analytical Solutions to Develop Finite Difference Scheme

Sturm-Liouville problems arrive very often when one is working with the equations of heat transfer. We provide the reader with a brief introduction to the theories and concepts relevant to the analytical solution of these PDEs. For a more in depth analysis of these equations we refer the reader to [26], [23], [51].

A Sturm-Liouville problem on a bounded domain $a < z < b$ is of the form

$$(s(z)u_z(z))' + q(z)u(z) = \lambda \sigma(z)u(z), \tag{A.1}$$

subject to the boundary conditions

$$\alpha_1 u(a) - \alpha_2 u'(a) = 0, \tag{A.2}$$

$$\beta_1 u(b) + \beta_2 u'(b) = 0. \tag{A.3}$$

Sturm-Liouville problems have several interesting properties of great importance. One such property is that they have an infinite number of eigenfunctions $u_1, u_2, ..., u_n, u_{n+1}...$ each corresponding to a different eigenvalue $\lambda_1, \lambda_2, ..., \lambda_n, \lambda_{n+1}....$ [45] Furthermore if $n \neq m$ then the eigenfunctions u_n and u_m are orthogonal with respect to the weight function $\sigma(z)$. [45]

$$\int_a^b u_n(z)u_m(z)\sigma(z)dz = 0; n \neq m. \tag{A.4}$$

In order to express a function $f(z)$ in terms of the eigenfunctions series we seek a superposition of these solutions which satisfies our boundary and initial conditions. This is done by finding constant multiples c_n of each term in the series so that the initial condition is represented as a Fourier series.

$$f(z) = \sum_{n=1}^{\infty} c_n u_n(z); a < z < b. \tag{A.5}$$

Multiplying both sides of this equation by $u_m(z)\sigma(z)$ and integrating over the domain we find that

$$\int_a^b f(z)u_m(z)\sigma(z)dz = \sum_{n=1}^{\infty} \int_a^b c_n u_n(z)u_m(z)\sigma(z)dz. \tag{A.6}$$

We know that u_n and u_m are orthogonal and thus the equation reduces to

$$\int_a^b f(z)u_m(z)\sigma(z)dz = c_m \int_a^b u_m^2(z)\sigma(z)dz. \tag{A.7}$$

We now obtain an equation for c_m as

$$c_m = \frac{\int_a^b f(z)u_m(z)\sigma(z)dz}{\int_a^b u_m^2(z)\sigma(z)dz}. \tag{A.8}$$

There are many texts on Sturm-Liouville problems and we refer the reader to [45] for an in depth analysis of these equations.

A.1 Heat Equation

Beginning with the heat conduction equation A.9 for a finite uniform rod defined on $0 < z < L$ and $0 < t$ where u is a function of z and t and boundary conditions (A.10) and (A.11).

$$u_t = \alpha u_{zz}, \tag{A.9}$$

$$u(0,t) = 1, \tag{A.10}$$

$$u_z(L,t) = 0, \tag{A.11}$$

$$u(z,0) = \cos\left(\frac{2\pi}{L}z\right). \tag{A.12}$$

For simplicity we allow $\alpha = 1$, however it is not difficult to incorporate a different value into the equation. As time approaches infinity, based on knowledge of diffusion, we expect the diffusion process to complete itself when an equilibrium is reached. Thus we seek to find a solution which is not dependent on time, commonly referred to as the steady state solution. To achieve this goal we allow $u(z,t) = w(z,t) + v(z)$, which still satisfies the above differential equation. Our system of equations now becomes

$$v_{zz} = 0, \tag{A.13}$$

,subject to the boundary conditions

$$v(0) = 1, \tag{A.14}$$

$$v_z(L) = 0, \tag{A.15}$$

and
$$w_t = w_{zz}, \tag{A.16}$$
subject to the boundary conditions
$$w(0) = 0, \tag{A.17}$$
$$w_z(L) = 0. \tag{A.18}$$

It is readily checked that the boundary conditions still reflect the original equation. Solving equation (A.13) by direct integration we find that

$$v(z) = Az + B. \tag{A.19}$$

Utilizing the boundary conditions on v we find that $B = 1$ and $A = 0$, and thus have a constant Steady State solution of
$$v(z) = 1. \tag{A.20}$$

This is exactly the type of solution one would expect to find in a perfectly insulated bar with one end kept at constant temperature. In fact if the boundary condition at $z = 0$ is s.t. $u(0,t) = T_0$ coupled with no flux conditions at $z = L$ then our solution would be $v(z) = T_0$ for the heat conduction problem.

Next we examine the time dependent solution $w(z,t)$. We allow the solution $w(z,t) = Z(z)T(t)$, a method known as separation of variables. Applying this expansion to our equation (A.16) we can isolate the z and t dependent terms on either side, implying that the R.H.S. and the L.H.S. must be equal to some constant. Since this constant can take any value we define a positive constant λ^2 such that

$$\frac{T'(t)}{T(t)} = \frac{Z''(z)}{Z(z)} = \pm\lambda^2. \tag{A.21}$$

Which yields a system of equations

$$Z''(z) \pm \lambda^2 Z(z) = 0, \tag{A.22}$$

$$T'(t) \pm \lambda^2 T(t) = 0, \tag{A.23}$$

with the boundary conditions

$$Z(0)T(t) = 0, \tag{A.24}$$

$$Z'(L)T(t) = 0. \tag{A.25}$$

Next we must examine the three cases for values of lambda. Since our boundary conditions are z dependent and $T(t) = 0$ yields only trivial solutions, we examine them with respect to our equation for $Z(z)$.

Case 1: $\lambda^2 = 0$

For this case we achieve the equation

$$Z''(z) = 0. \tag{A.26}$$

36

This case is similar to our Steady State solution, with the exception of different boundary conditions for $v(z,t)$. Thus this solution yields only the trivial solution and is omitted.

Case 2: λ^2 is positive

For this case our equation becomes

$$Z''(z) - \lambda^2 Z(z) = 0. \tag{A.27}$$

which has the solution

$$Z(z) = A\sinh(\lambda z) + B\cosh(\lambda z). \tag{A.28}$$

Once again utilizing the Boundary conditions we find that $B = 0$ and $A = 0$. Since again we find only trivial solutions, we omit the possibility that λ^2 is positive.

Case 3: λ^2 is negative

$$Z''(z) + \lambda^2 Z(z) = 0. \tag{A.29}$$

This equation has the solution

$$Z(z) = A\cos(\lambda z) + B\sin(\lambda z). \tag{A.30}$$

Solving the boundary conditions we find that $A = 0$ and that

$$Z'(L) = 0 = B\lambda\cos(\lambda L). \tag{A.31}$$

For a non-trivial solution to this equation (i.e. $B \neq 0$) we require that

$$\lambda_n = \frac{(2n-1)\pi}{2L}. \tag{A.32}$$

where $n \in \mathbb{N}$. We note here that equation (A.27) is a Sturm-Liouville problem with $s(z) = 1$, $q(z) = 0$, and $\sigma(z) = 1$. We have thus found an infinite number of solutions to the equation, as expected for a Sturm-Liouville problem. The solution for $T(t)$ thus is

$$T_n(t) = e^{-\lambda_n t}. \tag{A.33}$$

Our solution is now of the form

$$w_n(z,t) = B_n \sin\left(\frac{(2n-1)\pi z}{2L}\right) e^{-\frac{(2n-1)\pi}{2L}t}. \tag{A.34}$$

Now we wish to utilize the orthogonality principle to find the coefficients of the Fourier Series representation of our initial condition. Since our initial condition is $u(z,0) = w(z,0) + v(0) = \cos\left(\frac{2\pi}{L}\right)$, then $w(z,0) = \cos\left(\frac{2\pi}{L}\right) - v(0) = \cos\left(\frac{2\pi}{L}\right) - 1$.

$$B_n = \frac{\int_0^L \left(\cos\left(\frac{2\pi}{L}\right) - 1\right)\sin\left(\frac{(2n-1)\pi z}{2L}\right) dz}{\int_0^L \sin\left(\frac{(2n-1)\pi z}{2L}\right)^2}. \tag{A.35}$$

which for $L = 1$ has the solution

$$B_n = \frac{64}{\pi(8n^3 - 12n^2 - 26n + 15)}. \tag{A.36}$$

Thus the final solution for $u(z,t)$ is

$$u(z,t) = 1 + \sum_{n=1}^{\infty} \frac{64}{\pi(8n^3 - 12n^2 - 26n + 15)} \sin\left(\frac{(2n-1)\pi z}{2L}\right) e^{-\frac{(2n-1)\pi}{2L}t}. \tag{A.37}$$

A.2 Heat Equation With Advective Term

We expand the generalized heat equation (A.9) to incorporate an advective term giving us the new equation on the domain $0 < z < L$; $0 < t$:

$$u_t(z,t) + u_z(z,t) = \alpha u_{zz}(z,t). \tag{A.38}$$

In the non-dimensionalized equations we will be looking at, we have that $\alpha = \frac{1}{\mathbf{Pe}}$ and thus we express this equation as

$$\mathbf{Pe}\, u_t + \mathbf{Pe}\, u_z = u_{zz}. \tag{A.39}$$

Again we are interested in a no-flux boundary condition at z=L and a constant temperature input at z=0, expressed as

$$u(0,t) = 1, \tag{A.40}$$

$$u_z(L,t) = 0, \tag{A.41}$$

subject to the initial condition

$$u(x,0) = e^{-z}. \tag{A.42}$$

Proceeding as before we seek to find first the steady state temperature distribution. Thus we split the solution into its parts $u(z,t) = w(z,t) + v(z)$, which still satisfies the differential equation. For the steady state solution we have that

$$\mathbf{Pe}\, v_z(z) = v_{zz}, \tag{A.43}$$

$$v(0) = 1, \tag{A.44}$$

$$v_z(L) = 0. \tag{A.45}$$

One solution to the S.S. equation (A.43) is simply $v(z) = A$, where A is a constant. Setting this equation to our boundary conditions we find that $A = 1$.

Now the transient problem is

$$\mathbf{Pe}\, w_t + \mathbf{Pe}\, w_z = w_{zz}, \tag{A.46}$$

$$w(0,t) = 0, \tag{A.47}$$

$$w_z(z,t) = 0. \tag{A.48}$$

Applying the method of seperation of variables we let $w(z,t) = Z(z)T(t)$ and thus our equation reduces down to

$$\mathbf{Pe}\, T'(t)Z(z) + \mathbf{Pe}\, Z'(z)T(t) = Z''(z)T(t), \tag{A.49}$$

which after dividing through by $Z(z)T(t)$ and rearanging yields

$$\mathbf{Pe}\, \frac{T'(t)}{T(t)} = \frac{Z''(z) - \mathbf{Pe}\, Z'(z)}{Z(z)} = \pm\lambda^2. \tag{A.50}$$

Since either side of the equation is dependent on only one variable they must be equal to some constant λ^2. In the same fashion as is done for the generalized heat equation we find that this value must be negative to yield a non-trivial solution. We can now split equation (A.50) into two different equations

$$Z''(z) - \mathbf{Pe}\, Z'(z) + \lambda^2 Z(z) = 0, \tag{A.51}$$

$$\mathbf{Pe}\, T'(t) + \lambda^2 T(t) = 0. \tag{A.52}$$

Similarly our boundary equations become

$$Z(0)T(t) = 0, \tag{A.53}$$

$$Z'(L)T(t) = 0. \tag{A.54}$$

If we take equation (A.51) and multiply it by the function $\mu(z)$ it still satisifies the original equation.

$$\mu(z)Z''(z) - \mathbf{Pe}\,\mu(z)Z'(z) + \lambda^2\mu(z)Z(z) = 0. \tag{A.55}$$

To put this equation in Sturm-Lioville form we require that $\mu'(z) = -\mathbf{Pe}\,\mu(z)$, which implies that $\mu(z) = e^{-\mathbf{Pe}\,z}$, rendering

$$(\mu(z)Z'(z))' + \lambda^2\mu(z)Z(z) = 0. \tag{A.56}$$

We now have our equation in the form of equation (A.1) with $s(z) = \mu(z)$, $q(z) = 0$, and $\sigma(z) = \mu(z)$.

Since these boundary conditions are defined only on z-dependent boundaries we can reduce them to $Z(0) = 0$ and $Z'(L) = 0$, noting that $T(t)$ is bounded as temperature profile which approaches inf is not a realistic solution. Now we proceed with the solution of equation (A.51), as our boundary conditions are dependent on z. The characteristic equation for this problem is

$$r^2 - \mathbf{Pe}\, r + \lambda^2. \tag{A.57}$$

39

Table A.1: First 27 Eigenvalues λ_n

0.09335928962935758	0.5955701750798484	1.595821335413050	3.095893555617073
5.095923678041919	7.595939016997393	10.59594786715259	14.09595343021979
18.09595715267296	22.59595976493730	27.59596166821427	33.09596309751221
39.09596419802944	45.59596506364559	52.59596575617613	60.09596631949995
68.09596678343551	76.59596717017770	85.59596749594653	95.09596777291552
105.0959680103653	115.5959682141146	126.5959683949113	138.0959685487121
150.0959686861487	162.5959688077412	175.5959689158349	

Solving the quadratic we find that

$$r = \frac{\mathbf{Pe} \pm \sqrt{\mathbf{Pe}^2 - 4\lambda^2}}{2}. \tag{A.58}$$

Under the assumption that $\mathbf{Pe} \ll 1$ we assume that this has imaginary solutions

$$r = \frac{\mathbf{Pe} \pm i\sqrt{4\lambda^2 - \mathbf{Pe}^2}}{2}, \tag{A.59}$$

and a solution to equation (A.51) becomes

$$Z(z) = e^{\frac{\mathbf{Pe}}{2}} \left(A\cos\left(\frac{\sqrt{4\lambda^2 - \mathbf{Pe}^2}}{2}z\right) + B\sin\left(\frac{\sqrt{4\lambda^2 - \mathbf{Pe}^2}}{2}z\right) \right). \tag{A.60}$$

Utilizing our boundary conditions we find that $A = 0$ and that

$$Z'(L) = 0 = Be^{\frac{\mathbf{Pe}}{2}L} \left(\frac{\mathbf{Pe}}{2}\sin\left(\frac{\sqrt{4\lambda^2 - \mathbf{Pe}^2}}{2}L\right) + \frac{\sqrt{4\lambda^2 - \mathbf{Pe}^2}}{2}\cos\left(\frac{\sqrt{4\lambda^2 - \mathbf{Pe}^2}}{2}L\right) \right). \tag{A.61}$$

Clearly $e^{\frac{\mathbf{Pe}}{2}L} \neq 0$ and $B = 0$ only leads to the trivial solution. Therefore the interior of the paranthesis must equal 0. At this stage we must assign values to both $\mathbf{Pe}$ and L as we must approximate the eigenvalues which satisfy equation (A.62). Letting $\mathbf{Pe} = \frac{1}{6}$ and $L = 2\pi$ we find that there is an infinite number of solutions to the following equation

$$\tan\left(\sqrt{4\lambda_n^2 - \mathbf{Pe}^2}\,\pi\right) = -\frac{\sqrt{4\lambda_n^2 - \mathbf{Pe}^2}}{\mathbf{Pe}}. \tag{A.62}$$

To solve the λ_n^2 roots of this equation we utilize Newton's Method. The first several terms of λ_n^2 are given in table A.1.

We then utilize equation (A.8) to determine the constants via the Maple platform. Due to the length of the recursion relation we omit the final solution here, however you may find this recursion in the code located at the end of the appendix. For equation (A.52) we find the solution

$$T(t) = e^{-\frac{\lambda_n^2}{\mathbf{Pe}}}. \tag{A.63}$$

40

A.3 Nusselt Term

We further expand upon this problem to incorporate a heat source term as can be found in our perturbation problem for Peclet $O(\delta^2)$ and Nusselt $O(\delta^2)$. We begin with the equation and B/Cs

$$\mathbf{Pe}\, u_t(z,t) + \mathbf{Pe}\, u_z(z,t) = u_{zz}(z,t) - \mathbf{Nu}\, u(z,t) \tag{A.64}$$

defined on $0 < z < 2\pi$ and $t > 0$.

$$u(0,t) = 1. \tag{A.65}$$

$$u_z(L,t) = 0. \tag{A.66}$$

Similar to the other problems we allow $u(z,t) = \hat{w}(z,t) + v(z)$ where $v(z)$ takes on the same boundary conditions as the prior example. However, the addition of the $\mathbf{Nu}\, u(z,t)$ no longer allows for $v(z) = T_0$ to be a solution.

$$v_{zz} - \mathbf{Pe}\, v_z - \mathbf{Nu}\, v = 0. \tag{A.67}$$

Our characteristic equation for this problem becomes

$$r^2 - \mathbf{Pe}\, r - \mathbf{Nu} = 0, \tag{A.68}$$

which reduces to the quadratic equation

$$r = \frac{\mathbf{Pe} \pm \sqrt{\mathbf{Pe}^2 + 4\,\mathbf{Nu}}}{2}. \tag{A.69}$$

The solution to this differential equation is now

$$v(z) = e^{\frac{\mathbf{Pe}}{2}z}\left(A\cosh\left(\frac{\sqrt{\mathbf{Pe}^2 + 4\,\mathbf{Nu}}}{2}z\right) + D\sinh\left(\frac{\sqrt{\mathbf{Pe}^2 + 4\,\mathbf{Nu}}}{2}z\right)\right). \tag{A.70}$$

To solve the above for our boundary condition, we insert values for $\mathbf{Pe}$ and $\mathbf{Nu}$. We thus define $\mathbf{Pe} := \frac{1}{6}$ and $\mathbf{Nu} := 4$. Utilizing our boundary conditions, noting that $L = 2\pi$ we find that $A = 1$ and that $D \approx -0.999999999978104$. Next we expand $\hat{w}(z,t) = w(z,t)e^{-\frac{\mathbf{Nu}}{\mathbf{Pe}}t}$ and the equation becomes

$$\mathbf{Pe}\, w_t e^{-\frac{\mathbf{Nu}}{\mathbf{Pe}}t} - \mathbf{Nu}\, w e^{-\frac{\mathbf{Nu}}{\mathbf{Pe}}t} + \mathbf{Pe}\, w_z e^{-\frac{\mathbf{Nu}}{\mathbf{Pe}}t} = w_{zz}e^{-\frac{\mathbf{Nu}}{\mathbf{Pe}}t} - \mathbf{Nu}\, w e^{-\frac{\mathbf{Nu}}{\mathbf{Pe}}t}. \tag{A.71}$$

which further reduces to

$$\mathbf{Pe}\, w_t = w_{zz} - \mathbf{Pe}\, w_z. \tag{A.72}$$

The resulting equation is exactly that for the time dependent case we presented in equation (A.46). Therefore after proceeding through the steps above we achieve the following equations.

$$Z_n(z) = e^{\frac{\mathbf{Pe}}{2}z}B_n \sin\left(\frac{\sqrt{4\lambda_n - \mathbf{Pe}^2}}{2}z\right), \tag{A.73}$$

41

$$T_n(t) = e^{-\lambda_n t}. \tag{A.74}$$

$$
\begin{aligned}
Z_n'(2\pi) &= 0. \\
&= B_n e^{\frac{\mathbf{Pe}}{2}z} \left(\frac{\mathbf{Pe}}{2} \sin\left(\frac{\sqrt{4\,\mathbf{Pe}\,\lambda_n - \mathbf{Pe}^2}}{2} z \right) + \frac{\sqrt{4\,\mathbf{Pe}\,\lambda_n - \mathbf{Pe}^2}}{2} \cos\left(\frac{\sqrt{4\,\mathbf{Pe}\,\lambda_n - \mathbf{Pe}^2}}{2} z \right) \right).
\end{aligned} \tag{A.75}
$$

We note here the equality between the differential equation (A.72) and (A.46) implying the eigenvalues λ_n are the same as those found in table A.1

To solve for B_n we notice that for initial condition $u(z,0) = 0 = \hat{w}(z,0) + v(z)$ we have that $\hat{w}(z,0) = w(z,0) = -v(z)$. Noting that $\sigma(z) = e^{-\mathbf{Pe}z}$ we must solve

$$
B_n = \frac{-\int_0^{2\pi} v(z) e^{\frac{\mathbf{Pe}}{2}z} \sin\left(\frac{\sqrt{4\,\mathbf{Pe}\,\lambda_n - \mathbf{Pe}^2}}{2} z \right) e^{-\mathbf{Pe}z}}{\int_0^{2\pi} \left(e^{\frac{\mathbf{Pe}}{2}z} \sin\left(\frac{\sqrt{4\,\mathbf{Pe}\,\lambda_n - \mathbf{Pe}^2}}{2} z \right) \right)^2 e^{-\mathbf{Pe}z}}. \tag{A.76}
$$

Thus the final solution to this equation takes the form

$$
\begin{aligned}
u(z,t) &= e^{\frac{\mathbf{Pe}}{2}z} \left(\cosh\left(\frac{\sqrt{Pe^2 + 4\,\mathbf{Nu}}}{L} z \right) + D \sinh\left(\frac{\sqrt{Pe^2 + 4\,\mathbf{Nu}}}{L} z \right) \right) \\
&\quad + \sum_{n=1}^{\infty} e^{\frac{\mathbf{Pe}}{2}z} B_n \sin(n\pi z) e^{-\left(\frac{\mathbf{Nu}}{\mathbf{Pe}} + \lambda_n \right)t}.
\end{aligned} \tag{A.77}
$$

Appendix B

Computational Approaches

B.1 Forward Euler Method

Often times when modeling differential equations it becomes useful to consider discretization schemes to approximate the solution of these equations. In particular when an equation has no analytical solution these methods become essential to understanding how these equations operate. One such discretization scheme is the Forward Euler method. For the parabolic PDE

$$\frac{\partial u}{\partial t}(z,t) = \alpha \frac{\partial^2 u}{\partial z^2}, \tag{B.1}$$

defined on $0 < z < L$ and $t > 0$ and subject to the following boundary and initial conditions

$$u(0,t) = u(L,t) = 0, \tag{B.2}$$

$$u(z,0) = f(z). \tag{B.3}$$

We select an integer value $n > 0$ to define the spacial steps $\triangle z = \frac{L}{n}$ and a constant time-step size $\triangle t > 0$. In selecting these values we define a grid in both space and time on which we approximate the values of equation (B.1). This grid is thus defined as the set of points (z_i, t_j) where $z_i = i \triangle z$ for $i = 0, 1, 2, ..., n-1, n$ and $t_j = j \triangle t$ for $j = 0, 1, 2, ...$

We then expand the derivatives in equation (B.1) by using the Taylor series in their respective variables to obtain

$$\frac{\partial u}{\partial t}(z_i, t_j) = \frac{u(z_i, t_j + \triangle t) - u(z_i, t_j)}{\triangle t} - \frac{\triangle t}{2} \frac{\partial^2 u}{\partial t^2}(z_i, \zeta_j), \tag{B.4}$$

$$\frac{\partial^2 u}{\partial z^2} = \frac{u(z_i + \triangle z, t_j) - 2u(z_i, t_j) + u(z_i - \triangle z, t_j)}{(\triangle z)^2} - \frac{(\triangle z)^2}{12} \frac{\partial^4 u}{\partial z^4}(\xi_i, t_j), \tag{B.5}$$

where $\zeta_j \in (t_j, t_{j+1})$ and $\xi_i \in (z_{i-1}, z_{i+1})$.

Thus the difference method uses the difference of the quotients in equation (B.4) and (B.5) to approximate the solution $w_{i,j}$ of $u(z_i, t_j)$ in the equation (B.1). Our approximation equation now becomes

$$\frac{w_i^{j+1} - w_i^j}{\triangle t} - \alpha \frac{w_{i+1}^j - 2w_i^j + w_{i-1}^j}{(\triangle z)^2} = 0, \tag{B.6}$$

where the superscripts j and $j+1$ refer to the respective time steps and are not to be confused with exponents.

The first time step, $j = 0$ is given by the initial condition $w_i^0 = u(z_i, 0) = f(z_i)$. Isolating the next time step to one side of the equation we can then solve for the next time step based solely on information from the current step.

$$w_i^{j+1} = \left(1 - \frac{2\alpha \triangle t}{(\triangle z)^2}\right) w_i^j + \alpha \frac{\triangle t}{(\triangle z)^2} (w_{i+1}^j + w_{i-1}^j). \tag{B.7}$$

Defining the constant $\lambda = \alpha \frac{\triangle t}{(\triangle z)^2}$ we achieve the equation

$$w_i^{j+1} = (1 - 2\lambda)w_i^j + \lambda(w_{i+1}^j + w_{i-1}^j). \tag{B.8}$$

The coefficients of the R.H.S. of the equation (B.8) can be seen as the matrix A defined as

$$A = \begin{bmatrix} (1-2\lambda) & \lambda & 0 & \dots & & 0 \\ \lambda & (1-2\lambda) & \lambda & \ddots & & 0 \\ 0 & \ddots & \ddots & \ddots & & 0 \\ \vdots & & \ddots & \ddots & \ddots & \lambda \\ 0 & & \dots & 0 & \lambda & (1-2\lambda) \end{bmatrix}. \tag{B.9}$$

Letting $\mathbf{w}^0 = (f(z_1), f(z_2), ..., f(z_{n-1}))$ we can then define $\mathbf{w}^{j+1} = A\mathbf{w}^j$ for all $j \geq 0$. The Forward Euler Method thus is of order $O(\triangle t + (\triangle z)^2)$.

It may be noted that the Forward Euler method has unconditional instability [19].

B.2   Backward-Euler Method

Similar to the Forward-Difference scheme of section B.1 is the Backward-Difference Method or Backward-Euler Method. The backward method is an implicit method defined below.

$$\frac{\partial u}{\partial t}(z_i, t_j) = \frac{u(z_i, t_j) - u(z_i, t_j - \triangle t)}{\triangle t} + \frac{\triangle t}{2} \frac{\partial^2 u}{\partial t^2}(z_i, \zeta_j), \tag{B.10}$$

which allowing our approximation $w_i^j = u(z_i, t_j)$ results in the following scheme

$$\frac{w_i^j - w_i^{j-1}}{\triangle t} - \alpha \frac{w_{i+1}^j - 2w_i^j + w_{i-1}^j}{(\triangle z)^2} = 0. \tag{B.11}$$

Defining $\lambda = \alpha \frac{\triangle t}{(\triangle z)^2}$ this system reduces to

$$(1+2\lambda)w_i^j - \lambda w_{i+1}^j - \lambda w_{i-1}^j = w_i^{j-1}. \tag{B.12}$$

Defining the $(n-1) \times (n-1)$ matrix A as

$$A = \begin{bmatrix} (1+2\lambda) & -\lambda & 0 & \cdots & 0 \\ -\lambda & (1+2\lambda) & -\lambda & \ddots & 0 \\ 0 & \ddots & \ddots & \ddots & 0 \\ \vdots & \ddots & \ddots & \ddots & -\lambda \\ 0 & \cdots & 0 & -\lambda & (1+2\lambda) \end{bmatrix}. \tag{B.13}$$

we achieve the matrix representation as $A\mathbf{w}^j = \mathbf{w}^{j-1}$.

To show the stability of this method we utilize a Von Neumann Stability Analysis as described in [52]. We begin by letting the solution to $u(z,t) = \hat{u}(t)e^{ikz}$. Equation (B.12) reduces to equation (B.14).

$$(1+2\lambda)\hat{u}^j e^{ikz} - \lambda\hat{u}^j e^{ik(z+\triangle z)} - \lambda\hat{u}^j e^{ik(z-\triangle z)} = \hat{u}^{j-1}e^{ikz}. \tag{B.14}$$

Dividing equation (B.14) by e^{ikz} we arrive at the formulation in equation (B.15).

$$\begin{aligned} (1+2\lambda)\hat{u}^j - \lambda\hat{u}^j e^{ik\triangle z} - \lambda\hat{u}^j e^{-ik\triangle z} &= \hat{u}^{j-1}, \\ \Rightarrow \quad \hat{u}^j(1+2\lambda(1-\cos(k\triangle z))) &= \hat{u}^{j-1}, \\ \Rightarrow \quad \hat{u}^j(1-4\lambda\sin^2(\tfrac{k\triangle z}{2})) &= \hat{u}^{j-1}. \end{aligned} \tag{B.15}$$

In order to satisfy the stability of this equation we must have the inequality in equation (B.16) hold true.

$$\begin{aligned} \left| 1 - 4\lambda\sin^2\left(\tfrac{k\triangle z}{2}\right) \right| &\leq 1, \\ \Rightarrow \quad 0 \leq \lambda\sin^2\left(\tfrac{k\triangle z}{2}\right) &\leq \tfrac{1}{2}, \end{aligned} \tag{B.16}$$

$$0 \leq \sin^2\left(\frac{k\triangle z}{2}\right) \leq 1. \tag{B.17}$$

Due to the inequality in equation (B.17) we find that for stability of the Backwards Euler Method we must have that $0 \leq \lambda \leq \tfrac{1}{2}$.

B.3 Crank-Nicolson Method

Since the local truncation error of the Backward-Difference method has local truncation error of $O(\triangle t + (\triangle z)^2)$ then the time interval $\triangle t$ is required to be much smaller than the spatial interval $\triangle z$. It is thus useful to consider a system which has local truncation error of $O((\triangle t)^2 + (\triangle z)^2)$, which is exactly what we get when we average the Forward-Difference method at the jth step and the Backward-Difference method at the $(j+1)^{st}$ step. This averaging is referred to as the Crank-Nicolson method.

The resulting method gives

$$\frac{w_i^{j+1} - w_i^j}{\triangle t} = \alpha \left(\frac{w_{i+1}^j - 2w_i^j + w_{i-1}^j}{2(\triangle z)^2} + \frac{w_{i+1}^{j+1} - 2w_i^{j+1} + w_{i-1}^{j+1}}{2(\triangle z)^2} \right). \tag{B.18}$$

Defining λ as in the previous examples and isolating the $j+1$ and j terms we arrive at

$$w_i^{j+1} - \frac{\lambda}{2} \left(w_{i+1}^{j+1} - 2w_i^{j+1} + w_{i-1}^{j+1} \right) = w_i^j + \frac{\lambda}{2} \left(w_{i+1}^j - 2w_i^j + w_{i-1}^j \right), \tag{B.19}$$

or equivalently,

$$(1+\lambda)w_i^{j+1} - \frac{\lambda}{2} \left(w_{i+1}^{j+1} + w_{i-1}^{j+1} \right) = (1-\lambda)w_i^j + \frac{\lambda}{2} \left(w_{i+1}^j + w_{i-1}^j \right). \tag{B.20}$$

We consider this in its matrix form,

$$A\mathbf{w}^{j+1} = B\mathbf{w}^j, \tag{B.21}$$

where

$$A = \begin{bmatrix} (1+\lambda) & -\frac{\lambda}{2} & 0 & \dots & 0 \\ -\frac{\lambda}{2} & (1+\lambda) & -\frac{\lambda}{2} & \ddots & 0 \\ 0 & \ddots & \ddots & \ddots & 0 \\ \vdots & \ddots & \ddots & \ddots & -\frac{\lambda}{2} \\ 0 & \dots & 0 & -\frac{\lambda}{2} & (1+\lambda) \end{bmatrix}, \tag{B.22}$$

and,

$$B = \begin{bmatrix} (1-\lambda) & \frac{\lambda}{2} & 0 & \dots & 0 \\ \frac{\lambda}{2} & (1-\lambda) & \frac{\lambda}{2} & \ddots & 0 \\ 0 & \ddots & \ddots & \ddots & 0 \\ \vdots & \ddots & \ddots & \ddots & \frac{\lambda}{2} \\ 0 & \dots & 0 & \frac{\lambda}{2} & (1-\lambda) \end{bmatrix}. \tag{B.23}$$

Since A is positive definite, strictly diagonally dominant, and tri-diagonal it is nonsingular. A variety of methods can be used to produce the vector $\mathbf{w}^{j+1}$ from $\mathbf{w}^j$; however in MATLAB when A is a sparse matrix then the operation $A \backslash (B\mathbf{w}^j)$ returns the vector $\mathbf{w}^{j+1}$.

To show the stability of this method we utilize a Von Neumann Stability Analysis as described in (need ref). We begin by defining a solution to the differential equation (B.1) as $u(z,t) = \hat{u}(t)e^{ikz}$ due to the linearity of the equation. Equation (B.19) may now be expressed as in equation (B.24).

$$\hat{u}^{j+1}e^{ikz} - \frac{\lambda}{2} \left(\hat{u}^{j+1}e^{ik(z-\triangle z)} - 2\hat{u}^{j+1}e^{ikz} + \hat{u}^{j+1}e^{ik(z+\triangle z)} \right),$$
$$= \hat{u}^j e^{ikz} - \frac{\lambda}{2} \left(\hat{u}^j e^{ik(z-\triangle z)} - 2\hat{u}^j e^{ikz} + \hat{u}^j e^{ik(z+\triangle z)} \right). \tag{B.24}$$

Divinding equation (B.19) by e^{ikz} it may be expressed as in equation (B.25)

$$\hat{u}^{j+1}\left(1 - \tfrac{\lambda}{2}\left(e^{-ik\triangle z} - 2 + e^{ik\triangle z}\right)\right) = \hat{u}^{j}\left(1 + \tfrac{\lambda}{2}\left(e^{-ik\triangle z} - 2 + e^{ik\triangle z}\right)\right),$$

$$\Rightarrow \quad \hat{u}^{j+1}\left(1 + \lambda\left(1 - \cos(k\triangle z)\right)\right) = \hat{u}^{j}\left(1 - \lambda\left(1 - \cos(k\triangle z)\right)\right), \tag{B.25}$$

$$\Rightarrow \quad \hat{u}^{j+1} = \hat{u}^{j}\frac{1 - \lambda(1 - \cos(k\triangle z))}{1 + \lambda(1 - \cos(k\triangle z))} = \hat{u}^{j}\frac{1 - 2\lambda\sin^2\left(\frac{k\triangle z}{2}\right)}{1 + 2\lambda\sin^2\left(\frac{k\triangle z}{2}\right)}.$$

$$\left|\frac{1 - 2\lambda\sin^2\left(\frac{k\triangle z}{2}\right)}{1 + 2\lambda\sin^2\left(\frac{k\triangle z}{2}\right)}\right| \leq 1 \;,\; \forall \lambda > 0. \tag{B.26}$$

Due to the bound in equation (B.26) we have an unconditional stability in the Crank-Nicolson scheme as the relation in equation (B.27) holds true $\forall j \geq 0$.

$$\hat{u}_i^j = \hat{u}_i^{j-1}\frac{1 - 2\lambda\sin^2\left(\frac{k\triangle z}{2}\right)}{1 + 2\lambda\sin^2\left(\frac{k\triangle z}{2}\right)} = \hat{u}_i^0\left(\frac{1 - 2\lambda\sin^2\left(\frac{k\triangle z}{2}\right)}{1 + 2\lambda\sin^2\left(\frac{k\triangle z}{2}\right)}\right)^j. \tag{B.27}$$

B.4 Boundary Conditions

For homogeneous Dirichlet conditions s.t. $u(0,t) = T_0$ and $u(L,t) = T_1$ we have the same temperature prescribed at the endpoints of the rod for all times $t \geq 0$. It thus becomes unnecessary to calculate these endpoints within this discretization scheme, however these endpoints still affect the calculations at w_1^{j+1} and w_{n-1}^{j+1}, where n corresponds to the grid point $i = n$ at $z = L$. Thus a correction term must be added to both sides of equation (B.21) to include the boundary conditions.

$$A\mathbf{w}^{j+1} - \frac{\lambda}{2}\begin{bmatrix} T_0 \\ 0 \\ \vdots \\ 0 \\ T_1 \end{bmatrix} = B\mathbf{w}^{j} + \frac{\lambda}{2}\begin{bmatrix} T_0 \\ 0 \\ \vdots \\ 0 \\ T_1 \end{bmatrix}, \tag{B.28}$$

or,

$$A\mathbf{w}^{j+1} = B\mathbf{w}^{j} + \lambda\begin{bmatrix} T_0 \\ 0 \\ \vdots \\ 0 \\ T_1 \end{bmatrix}. \tag{B.29}$$

In the case where $T_0 = T_1 = 0$ this correction term is zero and results in equation (B.21).

Expanding on this concept if we wish to include Neumann boundary conditions of the form $u_z(L,t) = T_1$, we must utilize a central differencing of $\frac{\partial u}{\partial z}$.

$$\frac{\partial u}{\partial z}(n,t_j) = \frac{w_{n+1}^j - w_{n-1}^j}{2\,\triangle z} = T_1. \tag{B.30}$$

The grid point at $n+1$ is referred to as an image point. Utilizing this formulation of the z-derivative at $z = n$ we find that:

$$w_{n+1}^j = 2(\triangle z)T_1 + w_{n-1}^j. \tag{B.31}$$

When a no-flux boundary condition is applied at $z = L$ this implies that $T_1 = 0$ and thus $w_{n+1}^j = w_{n-1}^j$. Similarly at the $(j+1)$th time step $w_{n+1}^{j+1} = w_{n-1}^{j+1}$. Unlike the Dirichlet boundary conditions, we must now calculate the value of w_n for each time step $j > 0$. To accomplish this we expand the matrices A and B to be $n \times n$ matrices and multiply $A(n,n-1)$ and $B(n,n-1)$ by a factor of 2 to compensate for the image point.

$$A = \begin{bmatrix} (1+\lambda) & -\frac{\lambda}{2} & 0 & \dots & 0 \\ -\frac{\lambda}{2} & (1+\lambda) & -\frac{\lambda}{2} & \ddots & 0 \\ 0 & \ddots & \ddots & \ddots & 0 \\ \vdots & \ddots & -\frac{\lambda}{2} & \ddots & -\frac{\lambda}{2} \\ 0 & \dots & 0 & -\lambda & (1+\lambda) \end{bmatrix}, \tag{B.32}$$

and,

$$B = \begin{bmatrix} (1-\lambda) & \frac{\lambda}{2} & 0 & \dots & 0 \\ \frac{\lambda}{2} & (1-\lambda) & \frac{\lambda}{2} & \ddots & 0 \\ 0 & \ddots & \ddots & \ddots & 0 \\ \vdots & \ddots & \frac{\lambda}{2} & \ddots & \frac{\lambda}{2} \\ 0 & \dots & 0 & \lambda & (1-\lambda) \end{bmatrix}. \tag{B.33}$$

B.5 Generalized Heat Equation

We begin with the generalized Conservation Of Energy equation with $\alpha = 1$ defined on $0 \le z \le 1$ and $t > 0$ subject to the boundary conditions

$$u(0,t) = 1, \tag{B.34}$$

$$u_z(1,t) = 0. \tag{B.35}$$

The Crank-Nicolson scheme for this equation gives

$$A\mathbf{w}^{j+1} = B\mathbf{w}^j + \lambda \begin{bmatrix} 1 \\ 0 \\ \vdots \\ 0 \end{bmatrix}. \tag{B.36}$$

Table B.1: Table of Values For Convergence Comparissons

Case	$\triangle z = \frac{1}{10}$	$\triangle z = \frac{1}{100}$	$\triangle z = \frac{1}{200}$
$\lambda = 1$	$\triangle t = \frac{1}{100}$	$\triangle t = \frac{1}{10000}$	$\triangle t = \frac{1}{40000}$
$\lambda = \frac{1}{10}$	$\triangle t = \frac{1}{1000}$	$\triangle t = \frac{1}{100000}$	$\triangle t = \frac{1}{400000}$
$\lambda = \frac{1}{100}$	$\triangle t = \frac{1}{10000}$	$\triangle t = \frac{1}{1000000}$	$\triangle t = \frac{1}{4000000}$
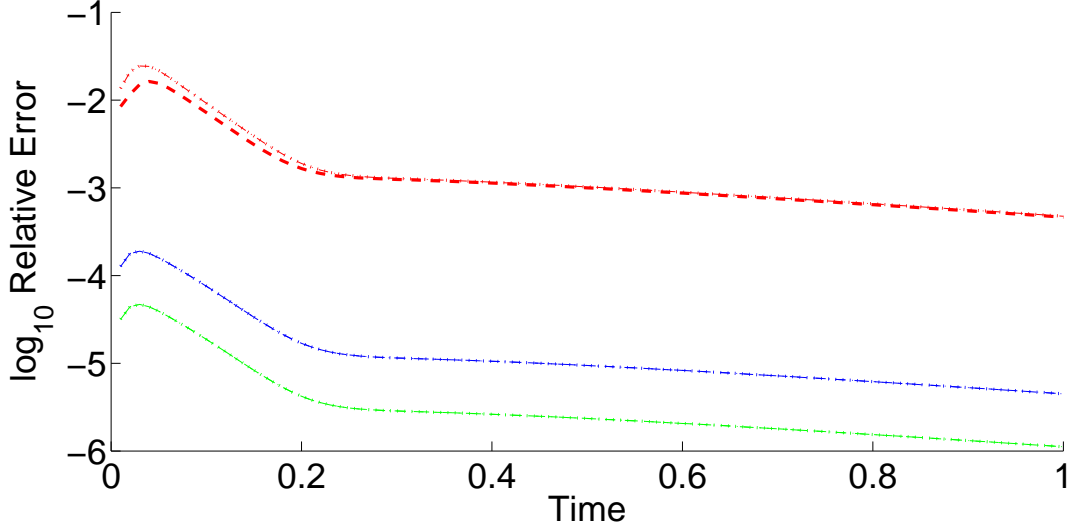
Figure B.1: Plots of C.N. approximations to equation (B.1) for values found in Table B.1. Red lines correspond to $\lambda = 1$, blue lines correspond to $\lambda = \frac{1}{2}$, and green lines correspond to $\lambda = \frac{1}{100}$. The lines for decreasing values of $\triangle t$ and $\triangle z$ while maintaining the same value of λ are virtually indistinguishable.

where A and B are the same as in equations (B.42) and (B.43).

We proceed to discretize this equation on several different grids of varying n and λ, which renders the following table for $\triangle t$ values.

Utilizing the analytical solutions found in section A.1 denoted u_a we calculate and plot $\frac{||w - u_a||_2}{||u_a||_2}$ at all points on the coarsest grid.

B.6 Crank-Nicolson with Upwinding

When we wish to consider the problem of heat transfer within a moving fluid we must expand upon the formulation of the problem in equation (B.1) to incorporate the advective term. Since the advective term can be seen as a flux term, the equation incorporating advection becomes

$$\mathbf{Pe}\frac{\partial u}{\partial t}(z,t) = \alpha \frac{\partial^2 u}{\partial z^2} - \mathbf{Pe}\frac{\partial u}{\partial z}. \tag{B.37}$$

To incorporate this term we utilize a method known as upwinding. We define the upwinding term approximation as

$$\frac{\partial u}{\partial z}(z_i, t_j) = \frac{w_i^j - w_{i-1}^j}{\triangle z}. \tag{B.38}$$

Averaging the Forward-Difference and Backward-Difference methods as was done in section (section) we render the approximation as

$$\frac{\partial u}{\partial z}(z_i, t_j) = \frac{w_i^j - w_{i-1}^j}{2\triangle z} + \frac{w_i^{j+1} - w_{i-1}^{j+1}}{2\triangle z}. \tag{B.39}$$

Thus we can express the difference formulation as

$$\mathbf{Pe}\,\frac{w_i^{j+1} - w_i^j}{\triangle t} + \mathbf{Pe}\,\frac{w_i^j - w_{i-1}^j}{2\triangle z} + \mathbf{Pe}\,\frac{w_i^{j+1} - w_{i-1}^{j+1}}{2\triangle z}$$

$$= \alpha\left(\frac{w_{i+1}^j - 2w_i^j + w_{i-1}^j}{2(\triangle z)^2} + \frac{w_{i+1}^{j+1} - 2w_i^{j+1} + w_{i-1}^{j+1}}{2(\triangle z)^2}\right). \tag{B.40}$$

Defining $\beta = \frac{\triangle t}{\triangle z}$ and λ as before our separated equation becomes

$$\mathbf{Pe}\,w_i^{j+1} - \frac{\lambda}{2}\left(w_{i+1}^{j+1} - 2w_i^{j+1} + w_{i-1}^{j+1}\right) + \mathbf{Pe}\,\frac{\beta}{2}\left(w_i^{j+1} - w_{i-1}^{j+1}\right)$$

$$= \mathbf{Pe}\,w_i^j + \frac{\lambda}{2}\left(w_{i+1}^j - 2w_i^j + w_{i-1}^j\right) - \mathbf{Pe}\,\frac{\beta}{2}\left(w_i^j - w_{i-1}^j\right). \tag{B.41}$$

which alters our matrix formulation $A\mathbf{w}^{j+1} = B\mathbf{w}^j + C$ to

$$A = \begin{bmatrix}
(\mathbf{Pe}+\lambda+\mathbf{Pe}\frac{\beta}{2}) & -\frac{\lambda}{2} & 0 & \cdots & 0 \\
-(\mathbf{Pe}\frac{\beta}{2}+\frac{\lambda}{2}) & (\mathbf{Pe}+\lambda+\mathbf{Pe}\frac{\beta}{2}) & -\frac{\lambda}{2} & \ddots & 0 \\
0 & \ddots & \ddots & \ddots & 0 \\
\vdots & \ddots & -(\mathbf{Pe}\frac{\beta}{2}+\frac{\lambda}{2}) & \ddots & -\frac{\lambda}{2} \\
0 & \cdots & 0 & -(\mathbf{Pe}\beta+\lambda) & (\mathbf{Pe}+\lambda+\mathbf{Pe}\frac{\beta}{2})
\end{bmatrix}. \tag{B.42}$$

and,

$$B = \begin{bmatrix}
(\mathbf{Pe}-\lambda-\mathbf{Pe}\frac{\beta}{2}) & \frac{\lambda}{2} & 0 & \cdots & 0 \\
(\frac{\lambda}{2}+\mathbf{Pe}\frac{\beta}{2}) & (\mathbf{Pe}-\lambda-\mathbf{Pe}\frac{\beta}{2}) & \frac{\lambda}{2} & \ddots & 0 \\
0 & \ddots & \ddots & \ddots & 0 \\
\vdots & \ddots & (\frac{\lambda}{2}+\mathbf{Pe}\frac{\beta}{2}) & \ddots & \frac{\lambda}{2} \\
0 & \cdots & 0 & (\lambda+\mathbf{Pe}\beta) & (\mathbf{Pe}-\lambda-\mathbf{Pe}\frac{\beta}{2})
\end{bmatrix}. \tag{B.43}$$
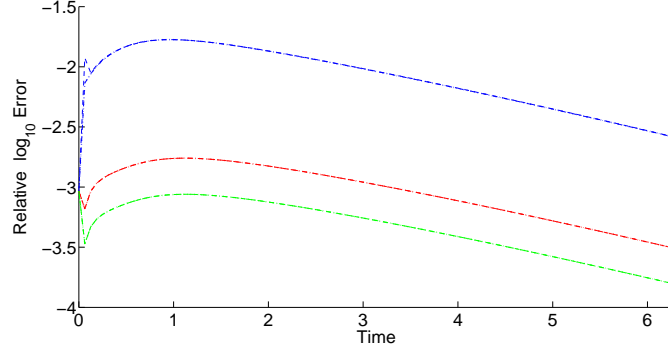
Figure B.2: $\log_{10}$ relative error $\frac{||u_a - w||}{||u_a||}$ for equation (B.47). Blue lines are *lambda* $= \frac{2\pi}{10}$, Red lines are $\lambda = \frac{2\pi}{100}$, Green lines are $\lambda = \frac{2\pi}{200}$. Once again notice there is close agreement between plots with equal values of λ.

$$C = (\lambda - \mathbf{Pe}\,\beta) \begin{bmatrix} 1 \\ 0 \\ \vdots \\ 0 \end{bmatrix} \tag{B.44}$$

Note that $A(n, n-1)$ and $B(n, n-1)$ have been altered for the no-flux boundary condition at $z_i = n$. Once again we created a Crank-Nicolson MATLAB model and graphed $\frac{||\mathbf{u}_a - \mathbf{w}||_2}{||\mathbf{u}_a||_2}$ as shown in Figure B.2. The values used in this plot are similar to those in table B.1 except that the boundary is now 2π as opposed to one. To compensate for this we also expand the stopping time to be 2π and thus all values of λ in this approximation correspond to $\frac{1}{2\pi}$ the value shown in the table, so that blue is $\lambda = \frac{1}{2\pi}$, red is $\frac{1}{20\pi}$, and green is $\frac{1}{200\pi}$.

B.7   Incorporation of $\mathbf{Nu}\,u(z,t)$

We further expand our Crank-Nicolson method to incorporate a 0th order term as can be found in our formulation of the problem (A.64) subject to the no-flux boundary condition $u_z(2\pi, t)$, $\forall t \geq 0$ and $u(0, t) = 1$, $\forall t \geq 0$.

For the term $\mathbf{Nu}\,u$ we average u in time as the Crank-Nicolson method is an averaging of the implicit and explicit methods at time steps j and $j+1$ respectively. Thus the term becomes

$$\mathbf{Nu}\,u(z_i, t_j) = \mathbf{Nu}\,\frac{w_i^{j+1} + w_i^j}{2} \tag{B.45}$$

The resulting equation (B.46) is similar to that in section B.6 except for the inclusion of this term.

51
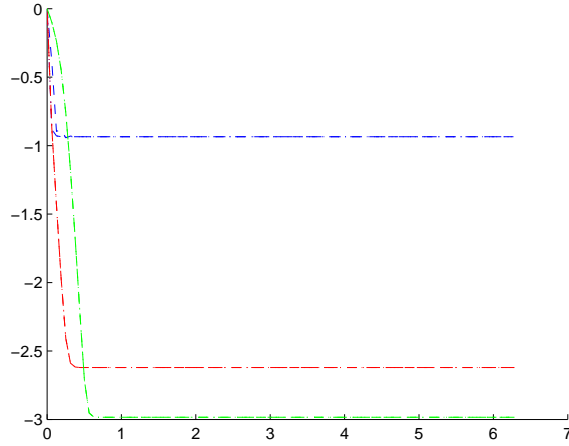
Figure B.3: $\log_{10}$ relative error $\frac{||u_a - w||}{||u_a||}$ for equation (A.77). Blue lines are $\lambda = \frac{2\pi}{10}$, Red lines are $\lambda = \frac{2\pi}{100}$, Green lines are $\lambda = \frac{2\pi}{200}$. Once again notice there is close agreement between plots with equal values of λ.

$$\mathbf{Pe}\, w_i^{j+1} - \frac{\lambda}{2}\left(w_{i+1}^{j+1} - 2w_i^{j+1} + w_{i-1}^{j+1}\right) + \mathbf{Pe}\,\frac{\beta}{2}\left(w_i^{j+1} - w_{i-1}^{j+1}\right) + \mathbf{Nu}\,\frac{\triangle t}{2}w_i^{j+1}$$

(B.46)

$$= \ \mathbf{Pe}\, w_i^{j} + \frac{\lambda}{2}\left(w_{i+1}^{j} - 2w_i^{j} + w_{i-1}^{j}\right) - \mathbf{Pe}\,\frac{\beta}{2}\left(w_i^{j} - w_{i-1}^{j}\right) - \mathbf{Nu}\,\frac{\triangle t}{2}w_i^{j} \qquad .$$

The same process for developing matrices A and B is used here, but omitted for brevity. It can be noted here that the correction terms are the same as those found in equation (B.44). Once again the plots are created for the relative error between the finite difference scheme and the analytical solution from section A.3 for an initial condition of $u(z,0) = 0$.

B.8   Code for equation (3.30)

To develop the code for equation (3.30) we allow the shape of the pipe to vary s.t. $h(z) = 1 + \varepsilon \sin(z)$.

$$\mathbf{Pe}\left(h(z)u_t + \frac{1}{12}u_z\right) - h'(z)u_z = h(z)u_{zz} - \mathbf{Nu}\,u$$

(B.47)

$$\mathbf{Pe}\,h_i w_i^{j+1} - h_i\tfrac{\lambda}{2}\left(w_{i+1}^{j+1} - 2w_i^{j+1} + w_{i-1}^{j+1}\right) + \left(\mathbf{Pe}\tfrac{\beta}{24} - h_i'\tfrac{\beta}{2}\right)\left(w_i^{j+1} - w_{i-1}^{j+1}\right) + \mathbf{Nu}\tfrac{\triangle t}{2}w_i^{j+1}$$

$$= \mathbf{Pe}\,h_i w_i^{j} + h_i\tfrac{\lambda}{2}\left(w_{i+1}^{j} - 2w_i^{j} + w_{i-1}^{j}\right) - \left(\mathbf{Pe}\tfrac{\beta}{24} - h_i'\tfrac{\beta}{2}\right)\left(w_i^{j} - w_{i-1}^{j}\right) - \mathbf{Nu}\tfrac{\triangle t}{2}w_i^{j} \qquad . \tag{B.48}$$

For this problem we have the terms h_i and h_i' which require a change to the matrix problem, where h_i and h_i' correspond to $h(z_i)$ and $h'(z_i)$ respectivelly.

$$\mathbf{Pe}\,h_i w_i^{j} = \mathbf{Pe}\left(1 + \sin\left(\frac{i2\pi}{n}\right)\right) I \mathbf{w}^{j}. \tag{B.49}$$

where I is the $(n \times n)$ identity matrix. In this manner the ith row of the identity matrix is element-wise multiplied by h_i.

For the advective term the coefficient matrix can no longer be represented as in equation (B.50) due to this element-wise multiplication.

$$\left(\mathbf{Pe}\frac{\beta}{24} - h_i\frac{\beta}{2}\right)\left(w_i^{j} - w_{i-1}^{j}\right) \tag{B.50}$$

This equation (B.50) must be split into two parts, that which include h_i and that which does not. We define the upwinding matrix term as the lower-diagonal matrix

$$U = \begin{bmatrix} 1 & 0 & 0 & \dots & 0 \\ -1 & 1 & 0 & \dots & \vdots \\ 0 & \ddots & -1 & 1 & \vdots \\ \vdots & \ddots & \ddots & \ddots & 0 \\ 0 & 0 & 0 & -1 & 1 \end{bmatrix}. \tag{B.51}$$

A new matrix must be created by multiplication of the ith row of UP by h_i rendering,

$$U2 = \begin{bmatrix} h_i' & 0 & 0 & \dots & 0 \\ -h_i' & h_i' & 0 & \dots & \vdots \\ 0 & \ddots & h_i'1 & h_i' & \vdots \\ \vdots & \ddots & \ddots & \ddots & 0 \\ 0 & 0 & 0 & -h_i' & h_i' \end{bmatrix}. \tag{B.52}$$

Now equation (B.50) can be represented as

$$\left(\mathbf{Pe}\frac{\beta}{24} - h_i'\frac{\beta}{2}\right)\left(w_i^{j} - w_{i-1}^{j}\right) = \mathbf{Pe}\frac{\beta}{24}U\mathbf{w}^{j} - \frac{\beta}{2}U2\mathbf{w}^{j} \tag{B.53}$$

Similarly, the diffusive term has the ith row of the corresponding coefficient matrix multiplied by h_i and the resulting code follows directly after.

Time Dependent Solver for (3.30)

```matlab
1 %% CN solver for Pe{h(z) T_t + 1/12 T_z} -  [h(z) T_z]_z +Nu T=0
2 % Pe O(d) and Nu O(d^2)
3 % BCs T(0,t)=1; T_z(L,t)=0;
4 % Init Cond T(z,0)=exp(-10z)
5 % This program is used to approx time dependent solution
6 clear; clc; close all;
7 %% Variable Declaration
8 variables=load ('param.par','-ASCII'); %data loaded from param.par files
9
10 k=variables(1);          %wavenumber from param
11 epsilon=variables(2);    %corrugation amplitude
12 Pe=variables(4);         %Pelet number
13 Nu=variables(3);         %Nusselt number
14 m=200;                   %number of time steps (used for dt)
15 n=100;                   %number of spatial steps (used for dz)
16 L=2*pi*k;                %length of pipe
17 maxtime=2*pi*k;          %used for dt (not a stop criteria)
18
19 dt=maxtime/m;            %dt
20 dz=L/n;                  %dz
21 lambda=dt/(dz^2);        %Coeff for D2 matrix
22 beta=dt/dz;              %Coeff for UP matrix
23
24 %% Initialize w, our approx.
25 w=zeros(n,2);            %set w to zeros
26 %% Declare Boundary Conditions
27 %requires w(0,t) & w(L,t)
28 BC0=1;                       %for value of BC at (0,t) (bottom of pipe)
29 BCL=0;                       %for value of BC at (L,t) (top of pipe)
30
31 %We can incorporate BCL directly into the D2 matrix thus BCL unused
32 %however we get additional correction terms for BC0 thus:
33
34 Corr=zeros(n,1);         %Holds the vector matrix for points off matrix
35 Corr(1,1)=BC0;           %For Diriclet cond. at z=0
36
37 if k==1
38     savenum=5;           %In case we want diff. saves for diff wave num
39 end
40 if k==10
41     savenum=5;
42 end
43 %% Declare Coeff Matrices
44
45 % D2 Matrix is tridiag main=-2 subdiags=1
46 % D2 is coefficient for u_zz approx.
47 % We now have h_i *(u_{i+1}-2u_{i}+2u_{i-1})
48 D2=zeros(n,n);
```

```
49 for i=2:1:n−1
50     D2(i,i)=−2;
51     D2(i,i+1)=1;
52     D2(i,i−1)=1;
53 end
54 D2(1,1)=−2;
55 D2(1,2)=1;
56 D2(n,n)=−2;
57 D2(n,n−1)=2;    %As B/C at L is u_z=0 we use image point
58
59 hprime=zeros(1,n);
60 % Solve matrix of derivative of corr. bound at each z_i
61 for i=1:1:n
62     hprime(1,i) = epsilon * cos(i*dz);
63 end
64 % UP matrix is lower bi−diag w/ main=−1; subdiag=1
65 % UP is coeff for upwinding
66 % UP2 is coeff for upwinding dependent on h'(z)
67 UP=zeros(n,n);
68 UP2=zeros(n,n);
69 for i=2:1:n
70     UP(i,i)=1;
71     UP2(i,i)=hprime(1,i);
72     UP(i,i−1)=−1;
73     UP2(i,i−1)=−hprime(1,i);
74 end
75 UP(1,1)=1;
76 UP2(1,1)=hprime(1,1);
77
78
79 %% Declare Initial Condition
80 for i=1:1:n
81 w(i,1)=exp(−10*i*dz); % w(i,1)=f(z,0)=exp(−10*dz*i)
82 end
83
84 %% Fix our boundary h(z) at each z_i
85 h=zeros(n,1);                      %preallocate vector
86 for i=1:1:n
87     h(i,1)=1+epsilon*sin(i*dz);   %whatever we define our boundary to be
88     D2(i,:)=D2(i,:)*h(i,1);
89 end
90
91
92
93 %Diagh is for terms w/ I*(w(:,j).*h)
94 %Preserving the seperation of w we instead force
95 %Diagh(i,i)=h(i) and now have equal term Diagh*w(:,j)
96 Diagh=diag(h);
97
98
99 %% Main Loop
```

55

```matlab
100 %count=zeros(20,20);
101 %Setup The Matrix RHS (Right)then find the coeff left side (Left)
102 %Find w(:,n+1) by Left\Right (sparse matrix transpose mult.)
103
104 newnorm=1000;   %sentinel value set (used for stopping parameter
105 count=0;        %used to count iterations to check if we need to save
106 place=1;        %stores the save points for matrices
107 output(:,place)=w(:,1);
108 while newnorm>10^(-4)   %%loop through all timeframes in question
109     Right=(Pe*Diagh-Pe/24.0*beta*UP+beta/2*UP2+lambda/2.0*D2-dt/2*Nu*eye...
            (n,n))*w(:,1)+(Pe*beta/12-hprime(1,1)*beta+lambda*D2(1,2))*Corr;
110     Left=(Pe*Diagh+Pe/24.0*beta*UP-beta/2*UP2-lambda/2.0*D2+dt/2*Nu*eye(...
            n,n));
111     w(:,2)=Left\Right;  %Solve for temp at next timestep
112     newnorm=norm(w(:,2)-w(:,1),2)/norm(w(:,1),2); %check against last ...
            time step
113
114     w(:,1)=w(:,2);    %move solution back one column for next iteration
115     count=count+1;    %one more iteration happened so count it
116
117     if count==savenum  %this is a savepoint
118         place=place+1; %this is position is output matrix to save
119         output(:,place)=w(:,1);  %now we save it
120         count=0;        %reset our counter to 0
121     end
122     if newnorm<10^(-8)    %save S.S. even if not a usual point
123         place=place+1;    %update save pos
124         output(:,place)=w(:,1);  %save it
125     end
126 end
127
128
129 save('data.mat','-v7.3'); %Save workspace data so plots can be created
130 %Another .m file cycles through these values and plots them
131 quit; %used for linux server batch files
```

Pe vs **Nu** Plot Solver for (3.30)

```matlab
 1 %% CN solver for Pe{h(z) T_t + 1/12 T_z} -  [h(z) T_z]_z +Nu T=0
 2 % Pe O(d) and Nu O(d^2)
 3 % BCs T(0,t)=1; T_z(L,t)=0;
 4 % Init Cond T(z,0)=exp(-10z)
 5 % This program is used to approx S.S. at end point for a range
 6 % of Peclet and Nusselt numbers
 7 clear; clc; close all;
 8 %% Variable Declaration
 9 variables=load ('param.par','-ASCII');  %Data stored in param files
10
11 k=variables(1);        %wavenumbers input from param.par
12 epsilon=variables(2);  %corr. amplitude input from param.par
```

```matlab
13 m=100;                       %number of time steps
14 n=10*k;                      %number of spatial steps (*k as we wish to ...
       preserve size of dz)
15 L=2*pi*k;                    %length of pipe in terms of num of corr.
16 maxtime=2*pi;               %Used for dt evern through it is not stopping ...
        requirement
17
18 dt=maxtime/m;               %dt
19 dz=L/n;                      %dz
20 lambda=dt/(dz^2);           %Coeff for D2
21 beta=dt/dz;                  %Coeff for UP
22
23 %% Initialize w, our approx.
24 w=zeros(n,m+1);             %w will store the approximate solution as w(z,t)
25 %% Declare Boundary Conditions
26 %requires w(0,t) & w(L,t)
27 BC0=1;  %for value of BC at (0,t) (bottom of pipe)
28 BCL=0;  %for value of BC at (L,t) (top of pipe) (unused BC)
29
30 %We can incorporate BCL directly into the D2 matrix however we get
31 %additional correction terms for BC0 thus:
32
33 Corr=zeros(n,1);            %Corr is for BCs outside of matrix (i.e. D2(1,0)...
       )
34 Corr(1,1)=BC0;
35
36
37 %% Declare Coeff Matrices
38
39 % D2 Matrix is tridiag main=-2 subdiags=1 which We now have h_i
40 % *(u_{i+1}-2u_{i}+2u_{i-1})
41 D2=zeros(n,n);
42 for i=2:1:n-1
43     D2(i,i)=-2;
44     D2(i,i+1)=1;
45     D2(i,i-1)=1;
46 end
47 D2(1,1)=-2;
48 D2(1,2)=1;
49 D2(n,n)=-2;
50 D2(n,n-1)=2; %As B/C at L is u_z=0 we use image point
51
52 hprime=zeros(1,n);
53 for i=1:1:n
54     hprime(1,i) = epsilon * cos(i*dz);
55 end
56 % UP matrix is lower bi-diag w/ main=-1; subdiag=1 for the advection ...
        term
57 % UP 2 is for the advective term with h'(z) coeff simply UP*h'(z)
58 UP=zeros(n,n);
59 UP2=zeros(n,n);
```

```matlab
60 for i=2:1:n
61     UP(i,i)=1;
62     UP2(i,i)=hprime(1,i);
63     UP(i,i−1)=−1;
64     UP2(i,i−1)=−hprime(1,i);
65 end
66 UP(1,1)=1;
67 UP2(1,1)=hprime(1,1);
68
69 Peclet=linspace(−2,2,20); %linspace of log10s, to use this val. we must ...
       use 10^Peclet(j)
70 Nusselt=linspace(−2,2,20); %linspace of log10s
71 output =zeros(20,20);
72
73
74 %% Declare Initial Condition
75 for i=1:1:n
76 w(i,1)=exp(−(i*dz)*10); % w(i,1)=f(z,0)=e^{−i*dz*10}
77 end
78 % Incorporate our boundry into the D2 matrix
79 h=zeros(n,1);
80 for i=1:1:n
81     h(i,1)=1+epsilon*sin(i*dz);   %whatever we define our boundary to be
82     D2(i,:)=D2(i,:)*h(i,1);
83 end
84
85
86 %h0=1+epsilon*sin(0*dz); %needed for BC (1 in this case)
87
88 %Diagh is for terms with I*(w(:,j).*h) Preserving the seperation of w we
89 %instead force Diagh(i,i)=h(i) and now have equal term Diagh*w(:,j)
90 Diagh=diag(h);
91
92
93 %% Main Loop
94 %count=zeros(20,20); Setup The Matrix RHS (R) Set the Right Hand Side of
95 %Equation Also not set for averaging Nu term
96
97 for out=1:1:20    %%Loop over Peclet values
98     for in=1:1:20  %%Loop over Nusselt Values
99
100 Pe=10^Peclet(out);            %Peclet number
101 Nu=10^Nusselt(in);            %Nusselt number
102
103
104 Right=zeros(n,1); %%RHS terms for iteration
105 Left=zeros(n,1); %%LHS terms for iteration
106 newnorm=10;
107
108 while newnorm>10^(−8)    %%loop through until S.S. approx. (newnorm ...
       compares relative w error w/ previous time step)
```

```matlab
109
110     Right=(Pe*Diagh-Pe/24.0*beta*UP+beta/2*UP2+lambda/2.0*D2-dt/2*Nu*eye...
            (n,n))*w(:,1)+(Pe*beta/12-hprime(1,1)*beta+lambda*D2(1,2))*Corr;
111     Left=(Pe*Diagh+Pe/24.0*beta*UP-beta/2*UP2-lambda/2.0*D2+dt/2*Nu*eye(...
            n,n));
112     w(:,2)=Left\Right;   %Sparse matrix division
113     newnorm=norm(w(:,2)-w(:,1),2)/norm(w(:,1),2);   %calculate rel. error
114
115     w(:,1)=w(:,2);   %move last temp to place 1
116     %count(out,in)=count(out,in)+1;   %Can be used to count iterations
117 end
118
119 output(out,in)=w(n,1);    %Store Steady State solution in output over ...
        various Pe and Nu
120
121     end
122 end
123
124
125 %A variety of different blotting options depending on desired use
126 %{
127 hold on plot(z,output(:,1),'g','LineWidth',2); hold on
128 plot(z,output(:,8),'--r','LineWidth',2); hold on;
129 plot(z,output(:,15),'-.b','LineWidth',2); hold on
130 plot(z,output(:,22),':m','LineWidth',2); hold on
131 plot(z,output(:,29),'y','LineWidth',2); hold on xlabel('z');
132 ylabel('T_{SS}(z)');
133 legend('\epsilon=0','\epsilon=0.2','\epsilon=0.4','\epsilon=0.6','\...
        epsilon=0.8');
134 %}
135
136 %%Plotting stuff
137 %{
138 hold on plot(z,output(:,1),'g','LineWidth',2); hold on
139 plot(z,output(:,2),'--r','LineWidth',2); hold on;
140 plot(z,output(:,3),'-.b','LineWidth',2); hold on
141 plot(z,output(:,4),':m','LineWidth',2); hold on
142 plot(z,output(:,5),'y','LineWidth',2); hold on
143 plot(z,output(:,6),'*c','LineWidth',2); hold on
144 plot(z,output(:,7),'og','LineWidth',2); xlabel('z'); ylabel('T_{SS}(z)')...
        ;
145 hold on plot(z,output(:,6),'*c','LineWidth',2);
146 legend('Pe=1/100','Pe=1/50','Pe=1/10','Pe=1','Pe=10','Pe=50','Pe=100');
147 %}
148
149
150 %{
151 hold on plot(z,output(:,1),'g','LineWidth',2); hold on
152 plot(z,output(:,2),'--r','LineWidth',2); hold on;
153 plot(z,output(:,3),'-.b','LineWidth',2); hold on
154 plot(z,output(:,4),':m','LineWidth',2); hold on
```

```
155 plot(z,output(:,5),'y','LineWidth',2); hold on
156 plot(z,output(:,6),'*c','LineWidth',2); hold on
157 plot(z,output(:,7),'og','LineWidth',2); xlabel('z'); ylabel('T_{SS}(z)')...
       ;
158 hold on plot(z,output(:,6),'*c','LineWidth',2);
159 legend('Nu=1/100','Nu=1/50','Nu=1/10','Nu=1','Nu=10','Nu=50','Nu=100');
160 %}
161 %{
162 x=linspace(min(Peclet),max(Peclet),200);
163 y=linspace(min(Nusselt),max(Nusselt),200); [xx,yy]=meshgrid(x,y); hold ...
       on
164 surf(xx,yy,interp2(Peclet,Nusselt,output,xx,yy,'linear')) ylabel('log_...
       {10}
165 Peclet') xlabel('log_{10}Nusselt')
166 %}
167 save('data.mat','-v7.3');   %Save data in file
168 quit;                       %For use with linux server param files
```

Crank-Nicolson Development for (A.9)

```
 1 %% Solve the problem Pe (u_t+u_z) = u_zz
 2 %Subject to BCs u(o,t)=1; u_z(2*pi,t)=0;
 3 %Initial condition set for u(z,0)=e^{-z}
 4 clear; clc; close all;
 5
 6 Pe=1/6;                     %Pe is the Peclet number
 7 L=2*pi;                     %L is the total length of the section in ...
       question
 8 maxtime=2*pi;               %stopping time criteria for CN
 9
10 zloop=[10,100,200];         %number of space steps for loop
11 tloop=[100,10000,40000];    %number of time steps for loops to preserve ...
       lambda values on each run
12
13
14 coarsen=zloop(1);           %coarsen stores our coarsest z dimension on ...
       grid
15 coarsem=tloop(1);           %coarsem stores coarsest t dimension on grid
16 coarsedz=L/coarsen;         %coarsedz is the Δ z value on coarsest grid
17 coarsedt=maxtime/coarsem;   %coarsedz is the Δ t value on coarsest grid
18
19
20
21 Error=zeros(9,tloop(1)+1);  %Error is to store the norm_2(Analytic-...
       Computational)/norm_2(Analytic)
22
23 %% Eigenvalues for problem with Pe=1/6
24 % Eigenvalues calculated using Newton's method for Pe=1/6 stored in eigs...
       .
25 eigs=[0.09335928962935758, 0.5955701750798484, 1.595821335413050, ...
```

```matlab
        3.095893555617073, 5.095923678041919, 7.595939016997393, ...
        10.59594786715259, 14.09595343021979, 18.09595715267296, ...
        22.59595976493730, 27.59596166821427, 33.09596309751221, ...
        39.09596419802944, 45.59596506364559, 52.59596575617613, ...
        60.09596631949995, 68.09596678343551, 76.59596717017770, ...
        85.59596749594653, 95.09596777291552, 105.0959680103653, ...
        115.5959682141146, 126.5959683949113, 138.0959685487121, ...
        150.0959686861487, 162.5959688077412, 175.5959689158349];
26 numofeig=size(eigs,2);   %numer of elements in eigs, stopping criterion ...
      for Analytic iterative
27
28 %% Main loop Begin
29 %In the main loop the value of dz changes on each succesion (see zloop)
30 %The function then calculates the analytic solution on the grid, then ...
      the
31 %CN approx, then determines norms as defined in Error.
32 %Nested loops are used to calculate these Error values for 3 different
33 %lambda cases.
34 for dzloop=1:1:3
35     n=zloop(dzloop);      %set new z-grid size
36     dz=L/n;               %calc dz
37     m=tloop(dzloop);      %set outermost loop for CN
38     a=10;                 %numer of points in between each dt for nested ...
           loop
39     b=10;                 %numer of points in between each dt for nested ...
           nested loop
40     %% Solve Analytic on Coarsest Grid
41     %Solves the analytical solution of the problem w/ given conditions:
42 Cn=zeros(1,numofeig);     %Cn is constant for each eigenvalue
43 A=zeros(1,numofeig);      %A(1,i) stores sqrt(4*eigs(1,i)-Pe^2) which ...
      appears often.
44 B=exp(-(Pe+2)*pi);        %Fixed value which appears often in Analytic ...
      solution
45 %Set the Cns
46 for count=1:1:numofeig
47     A(1,count)=sqrt(4*eigs(1,count)-Pe^2);
48     Cn(1,count)=-1/((Pe^2+4*Pe+4+A(1,count)^2)*(Pe^2+A(1,count)^2)*(2*A...
         (1,count)*pi-sin(2*A(1,count)*pi)));
49     Cn(1,count)=Cn(1,count)*(4*(4*A(1,count)*Pe+4*A(1,count)+A(1,count)*...
         B*cos(A(1,count)*pi)*Pe^2+A(1,count)^3*B*cos(A(1,count)*pi)+B*sin...
         (A(1,count)*pi)*Pe^3+B*sin(A(1,count)*pi)*Pe*A(1,count)^2+2*B*sin...
         (A(1,count)*pi)*Pe^2+2*B*sin(A(1,count)*pi)*A(1,count)^2-A(1,...
         count)*exp(-Pe*pi)*cos(A(1,count)*pi)*Pe^2-4*A(1,count)*exp(-Pe*...
         pi)*cos(A(1,count)*pi)*Pe-4*A(1,count)*exp(-Pe*pi)*cos(A(1,count)...
         *pi)-A(1,count)^3*exp(-Pe*pi)*cos(A(1,count)*pi)-Pe^3*exp(-Pe*pi)...
         *sin(A(1,count)*pi)-4*Pe^2*exp(-Pe*pi)*sin(A(1,count)*pi)-4*Pe*...
         exp(-Pe*pi)*sin(A(1,count)*pi)-Pe*exp(-Pe*pi)*sin(A(1,count)*pi)*...
         A(1,count)^2)*A(1,count));
50 end
51
52 %Set grid for Analytic solution
```

```matlab
53 wAnalytic=zeros(n+1,coarsem+1);
54
55 %Sum the terms of the fourier series for each gridpoint of coarsest grid
56 for j=1:1:coarsem+1
57     for i=1:1:n+1
58         for count=1:1:numofeig
59             wAnalytic(i,j)=wAnalytic(i,j)+Cn(1,count)*exp(Pe/2*dz*(i-1))...
                    *sin(A(1,count)*dz*(i-1)/2)*exp(-(eigs(1,count)/Pe)*...
                    coarsedt*(j-1));
60         end
61     end
62 end
63
64 %Trim the boundary at x=0 as it is always 1
65 wAnalytic(1,:)=[];
66 wAnalytic=wAnalytic+1;
67
68
69
70
71
72 %% Boundary condition Set
73 %BC holds the Boundary Condition at z=0;
74 BC=zeros(n,1);
75 BC(1,1)=1; %Boundary Condition at z=0 is constant 1
76 %% Set D2 and Up matrices
77
78 %D2*w is matrix representation of u_{zz} in CN
79 %UP*w is u_z matrix representation in CN
80 UP=zeros(n,n);
81 D2=zeros(n,n);
82
83 for i=2:1:n-1
84     D2(i,i)=-2;
85     D2(i,i-1)=1;
86     D2(i-1,i)=1;
87     UP(i,i)=1;
88     UP(i,i-1)=-1;
89 end
90 D2(1,2)=1;
91 D2(1,1)=-2;
92 D2(n,n-1)=2; %This is altered for no flux condition
93 D2(n,n)=-2;
94 D2(n-1,n)=1;
95 UP(1,1)=1;
96 UP(n,n-1)=-1;
97 UP(n,n)=1;
98
99
100
101 %% Set init condition
```

```matlab
102 %u(z,0)=exp(-z)
103 w1=zeros(n,m+1);     %Stores approximations of CN method for outermost ...
        loop (coarsest)
104 w2=zeros(n,a+1);     %Stores approximations of CN method for middle loop ...
        (finer)
105 w3=zeros(n,b+1);     %Stores approximations of CN method for inner loop (...
        finest)
106 %Set our initial condition to each w
107 for i=1:1:n
108     w1(i,1)=exp(-dz*i);
109     w2(i,1)=exp(-dz*i);
110     w3(i,1)=exp(-dz*i);
111 end
112 %Calculate our initial error
113 Error(:,1)=log10(norm(wAnalytic(:,1)-w1(:,1),2)/norm(wAnalytic(:,1),2));
114
115 %temp_ is used to count number of iterations for their respective loop
116 %ensuring we only calc Error on coarse grid.
117 %place_ is used to keep track of matrix position for Error
118 temp1=0;
119 temp2=0;
120 temp3=0;
121 place1=1;
122 place2=1;
123 place3=1;
124
125 %CN begins here
126 for j=1:1:m
127     dz=L/n;      %Set dz
128     dt=maxtime/m;   %dt needs to be reset as it changes in nested loops.
129     lambda=dt/(dz^2); %dt changes --> lambda changes
130     beta=dt/dz;         %" --> beta changes
131
132     %Right is the entirety of the Right hand side, LEFT is LHS/w(:,j+1)
133     RIGHT=(Pe*eye(n,n)+lambda/2*D2-Pe*beta/2*UP)*w1(:,j)+(lambda+Pe*beta...
            )*BC;
134     LEFT=(Pe*eye(n,n)-lambda/2*D2+Pe*beta/2*UP);
135     w1(:,j+1)=LEFT\RIGHT;   %Sparse matrix inverse mult operation
136     temp1=temp1+1;    %Increase temp as we step along t-axis
137     %Check to see if we hit a coarse grid point
138     if temp1==m/coarsem %Calculate Error
139         Error(1+(3*(dzloop-1)),place1+1)=log10(norm(wAnalytic(:,place1...
                +1)-w1(:,j+1),2)/norm(wAnalytic(:,place1+1),2));
140         temp1=0; %reset temp to 0 so our bool check for coarse grid ...
                operates
141         place1=place1+1; %Increase place counter
142     end
143
144     %Steps similar to above
145     for q=1:1:a
146         dt=maxtime/(m*a);
```

63

```
147          lambda=dt/(dz^2);
148          beta=dt/dz;
149          RIGHT=(Pe*eye(n,n)+lambda/2*D2−Pe*beta/2*UP)*w2(:,q)+(lambda+Pe*...
                 beta)*BC;
150          LEFT=(Pe*eye(n,n)−lambda/2*D2+Pe*beta/2*UP);
151          w2(:,q+1)=LEFT\RIGHT;
152          temp2=temp2+1;
153          if temp2==m*a/coarsem
154              Error(2+(3*(dzloop−1)),place2+1)=log10(norm(wAnalytic(:,...
                     place2+1)−w2(:,q+1),2)/norm(wAnalytic(:,place2+1),2));
155              temp2=0;
156              place2=place2+1;
157          end
158
159          for r=1:1:b
160              dt=maxtime/(m*a*b);
161              lambda=dt/(dz^2);
162              beta=dt/dz;
163              RIGHT=(Pe*eye(n,n)+lambda/2*D2−Pe*beta/2*UP)*w3(:,r)+(lambda...
                     +Pe*beta)*BC;
164              LEFT=(Pe*eye(n,n)−lambda/2*D2+Pe*beta/2*UP);
165              w3(:,r+1)=LEFT\RIGHT;
166              temp3=temp3+1;
167              if temp3==m*a*b/coarsem
168                  Error(3+(3*(dzloop−1)),place3+1)=log10(norm(wAnalytic(:,...
                         place3+1)−w3(:,r+1),2)/norm(wAnalytic(:,place3+1),2))...
                         ;
169                  temp3=0;
170                  place3=place3+1;
171              end
172          end
173          w3(:,1)=w3(:,r+1);    %move w3(:,r+1) to w3(:,1) so next ...
                 iteration of w3 loop picks up where it left off
174      end
175      w2(:,1)=w2(:,q+1);    %move w2(:,q+1) to w2(:,1) so next iteration ...
             of w2 loop picks up where it left off
176 end
177
178 end
179
180 %Set time vector for plot
181 time=linspace(0,maxtime,coarsem+1); %Plot times from 0 to maxtime
182
183 %Values of same dz have same color, style varies with lambda
184 hold on
185 plot(time,Error(1,:),'−−b');
186 hold on;
187 plot(time,Error(2,:),'−.b');
188 hold on
189 plot(time,Error(3,:),':b');
190 hold on
```

```matlab
191 plot(time,Error(4,:),'--r');
192 hold on
193 plot(time,Error(5,:),'-.r');
194 hold on
195 plot(time,Error(6,:),':r');
196 hold on
197 plot(time,Error(7,:),'--g');
198 hold on
199 plot(time,Error(8,:),'-.g');
200 hold on
201 plot(time,Error(9,:),':g');
202 hold on
```

Bibliography

[1] C. Ahheng, J. Dunbar, and T. Haufler. Impacts and limitations of residential geothermal heating systems, 2011.

[2] Soo Wahn Ahn. Experimental studies on heat transfer in the annuli with corrugated inner tubes. *KSME International Journal*, 17(8):1226–1233, 2003.

[3] R. Al-Khoury, P.G. Bonnier, and R.B.J. Brinkgreve. Efficient finite element formulation for geothermal heating systems. part i: Steady state. *International Journal for Numerical Methods in Engineering*, 63:988–1213, 2005.

[4] R. Al-Khoury, T. Kolbel, and R. Schramedei. Modelling of borehole heat exchangers. *Computers and Geosciences*, 36:1301–1315, 2010.

[5] A. Al-Sarkhi, S. Abu-Nada, E.and Nijmeh, and B. Akash. Performance evaluation of standing column well for potential application of ground source heat pump in jordan. *Energy Conversion and Management*, 49:863–872, 2008.

[6] Marita Allan. Geothermal heat pump grouting materials.

[7] Dale A. Anderson, John C. Tannehill, and Richard H. Pletcher. *Computational Fluid Mechanics and Heat Transfer*. McGraw-Hill Book Company, 1984.

[8] R. Aris. On the dispersion of a solute in a fluid flowing through a tube. *Royal Society of London Series A, MAthematical and Physical Sciences*, 235(1200):67–77, 1956.

[9] ASHRAE. Commercial/institutional ground source heat pump engineering manual. *American Society of Heating, Refrigerating and Air Conditioning Engineers, Inc.*, 1995.

[10] Tatyana V. Bandos, Alvaro Montero, Esther Fernandez, Juan Luis G. Santander, Jose Maria Isidiro, Jezabel Perez, Pedro J. Fernandez de Cordoba, and Javier F. Urchueguia. Finite line-source model for borehole heat exchangers: effect of vertical temperature variations. *Geothermics*, 38:263–270, 2009.

[11] Gopal Bandyopadhyay, William Gosnold, and Michael Mann. Analytical and semi-analytical solutions for short-term transient response of ground heat exchangers. *Energy and Buildings*, 40:1816–1824, 2008.

[12] Richard A. Beier. Vertical temperature profile in ground heat exchanger during in-situ test. *Renewable Energy*, 36:1578–1587, 2011.

[13] Richard Bellman. *Perturbation Techniques in Mathematics, Physics, and Enginnering*. Holt, Rinehart and Winston, Inc., 1964.

[14] Carl M. Bender and Steven A. Orszag. *Advance Mathematical Methods for Scientists and Engineers*. McGraw-Hill Book Company, 1978.

[15] Yuehong Bi, Lingen Chen, and Chih Wu. Ground source heat exchanger temperature distribution analysis and experimental verification. *Applied Thermal Engineering*, 22:183–189, 2002.

[16] Benny Bohm. On transient heat losses from buried district heating pipes. *International Journal of Energy Research*, 24:1311–1334, 2000.

[17] J. Boyer, S. Frei, K. Lockwood, and G. Stewart. Geometry and flow effects on the performace of residential geothermal heating systems. In *New England Geothermal Professional Association*. Research Experience for Undergraduates, 2011.

[18] David L. Brown, Donald Bell, John abd Estep, William Gropp, Bruce Hendrickson, Allie Keller-McNulty, David Keyes, J. Tinsley Oden, Linda Petzold, and Margaret Wright. On transient heat losses from buried district heating pipes, 2008.

[19] Richard L. Burden and FairesJ. Douglas. *Numerical Analysis Eighth Edition*. Brooks Cole, 2005.

[20] Michele De Carli, Massimo Tonon, Angelo Zarrella, and Roberto Zecchin. A computational capacity resistance model (carm) for vertical ground-coupled heat exchangers. *Renewable Energy*, 35:1537–1550, 2010.

[21] Hakan Demir, Ahmet Koyun, and Galip Temir. Heat transfer of horizontal parallel pipe ground heat exchanger and experimental verification. *Applied Thermal Energy*, 29:224–233, 2009.

[22] Hikmet Esen and Mustafa Inalli. In-situ thermal response test for ground source heat pump systems in elazig, turkey. *Energy and Buildings*, 41:395–401, 2009.

[23] Stanley J. Farlow. *Partial Differntial Equation for Scientists and Engineers*. John Wiley and Sons, 1982.

[24] Georgios Florides and Soteris Kalogirou. Ground heat exchangers-a review of systems models and applications. *Renewable Energy*, 32:2461–2478, 2007.

[25] David Goodstein. *Out of Gas: The End of the Age of Oil*. W.W. Norton & Company, 2004.

[26] Richard Haberman. *Elementary Applied Partial Differential Equations: With Fourier Series and Boundary Value Problems*. Prentice Hall, 1983.

[27] G. Iaccarino, A. Ooi, P. A. Durbin, and M. Behnia. Conjugate heat transfer predictions in two-dimensional ribbed passages. *International Journal of Heat and Fluid Flow*, 23:340–345, 2002.

[28] H. Iacovides and M. Raisee. Computation of flow and heat transfer in two-dimensional rib-roughened passages, using low-reynolds-number turbulence models. *International Journal of Numerical Methods for Heat and Fluid Flow*, 11:138–155, 2001.

[29] International Energy Agency. Renewable energy essentials: Geothermal. *Organization for Economic Cooperation*, 2010.

[30] Yusuf Ali Kara. Experimental performance evaluation of a closed-loop vertical ground source heat pump in the heating mode using energy analysis method. *International Journal of Energy Research*, 31:1504–1516, 2007.

[31] S. Kavanaugh. Containment for ground source heat pumps. *Report for Alabama Universities TVA Research Consortium*, December 1995.

[32] J. M. Kay. *An Introduction to Fluid Mechanics and Heat Transfer Second Edition*. Cambridge at the University Press, 1963.

[33] M.H. Khan and J.D. Spitler. Performance anaylsis of a residential ground source heat pump system with antifreeze solution, 2004.

[34] A. Koyun, H. Demir, and T. Zakir. Experimental study of heat transfer of buried finned pipe for ground source heat pump applications. *International Communications in Heat and Mass Transfer*, 36:739–743, 2009.

[35] L. Lamarche and B. Beauchamp. New contribution to the finite line-source model for geothermal boreholes. *Energy and Buildings*, 39:188–198, 2007.

[36] L. Lamarche and B. Beauchamp. New solutions for the short-time analysis of geothermal vertical boreholes. *International Journal of Heat and Mass Transfer*, 50:1408–1419, 2007.

[37] Michael L'Ecuyer, Cathy Zoi, and John S. Hoffman. Space conditioning: The next frontier. *Air and Radiation*, April 1993.

[38] X. Li, Z. Chen, and J. Zhao. Simulation and experiment on the thermal performance of u-vertical ground coupled heat exchanger. *Applied Thermal Engineering*, 26:1564–1571, 2006.

[39] P.J. Lienau. Geothermal heat pump performance and utility programs in the united states. *Energy Sources*, 19(1):1–8, 1997.

[40] Ben Luce. Heating your home or business in vermont with a geothermal system. *Northeast Vermont Development Association*, January 2011.

[41] Jason Massmann. How a geothermal system works. `http://www.massmanngeothermal.com/about\_geothermal.htm`, 2012.

[42] Michael J. Moran and Howard N. Shapiro. *Fundamentals of Engineering Thermodynamics 5th Edition*. John Wiley and Sons Inc., 2004.

[43] Gale A. Norton and Charles G. Groat. Geothermal energy-clean power from the earth's heat. U.S. Department of the Interior and U.S. Geological Survey, 2003.

[44] A. M. Omer. Ground-source heat pumps systems and applications. *Renewable and Sustainable Energy Reviews*, 12:344–371, 2008.

[45] David L. Powers. *Boundary Value Problems and Partial Differential Equations*. Elsevier.

[46] K. Rafferty. An information survival kit for the prospective geothermal heat pump owner. *Heatspring Energy*, March 2008.

[47] Regional Economic Research Inc. Ground source heat pump market assesment final report. *Northwest Energy Efficiency Alliance*, September 2000.

[48] Dietmar Rempfer. On boundary conditions for incompressible navier-stokes problems. *Applied Mechanics Reviews*, 59:107–125, 2006.

[49] Jeffrey D. Spitler, Andrew Chiasson, and Cenk Yavuzturk. Extension of existing design and simulation models. Department of Energy, 1996.

[50] Ivar Stakgold. *Green's Functions and Boundary Value Problems*. John Wiley and Sons, 1998.

[51] Walter A. Strauss. *Partial Differential Equations Second Edition*. John Wiley and Sons, 2008.

[52] Lambert M. Surhone. *Von Neumann Stability Analysis*. Betascript Publishing, 2010.

[53] Geoffrey Taylor. Dispersion of soluble matter in solvent flowing slowly through a tube. *Proceedings of the Royal Society of London. Series A, Mathematical and Physical Sciences*, 219(1137):186–203, 1953.

[54] Geoffrey Taylor. Conditions under which dispersion of a solute in a stream of solvent can be used to measure molecular diffusion. *Proceedings of the Royal Society of London. Series A, Mathematical and Physical Sciences*, 225(1163):473–477, 1954.

[55] G. Tyler Miller and Scott Spoolman. *Environmental Science*. Brooks Cole, 2010.

[56] U.S. Department of Energy. Report of the first quadrennial technology review. *DOE Quadrennial Review*, September 2011.

[57] U.S. Energy Information Administration. U.S. Energy Facts: Energy Explained. `http://www.eia.gov/energyexplained`, October 2011.

[58] Bogdan Vernescu and Chiang C. Mei. *Homogenization Methods for Multiscale Mechanics*. World Scientific, 2010.

[59] Yuxi Zheng. Partial differential equations. `http://www.math.psu.edu/yzheng/m597k/m597kLIII5.pdf`, 2010.